JGR Oceans

RESEARCH ARTICLE
10.1029/2023JC020691

Quantifying Biogeochemical Controls of Open Ocean CDOM From a Global Mechanistic Model

Kana Yamamoto[1], **Tim DeVries**[2,3], **David A. Siegel**[2,3], **and Norman B. Nelson**[2]

[1]Interdepartmental Graduate Program in Marine Science, University of California, Santa Barbara, CA, USA, [2]Earth Research Institute, University of California, Santa Barbara, CA, USA, [3]Department of Geography, University of California, Santa Barbara, CA, USA

Key Points:

- A budget for open ocean chromophoric dissolved organic matter (CDOM) is constructed using a two-component biogeochemical model
- An estimated 7% of open-ocean CDOM comes from rivers, and about 80% of marine-origin CDOM is derived from particulate organic matter
- Biological degradation dominates the loss of short-lived CDOM while photodegradation controls the fate of long-lived CDOM

Supporting Information:

Supporting Information may be found in the online version of this article.

Correspondence to:

K. Yamamoto,
kyamamoto@ucsb.edu

Citation:

Yamamoto, K., DeVries, T., Siegel, D. A., & Nelson, N. B. (2024). Quantifying biogeochemical controls of open ocean CDOM from a global mechanistic model. *Journal of Geophysical Research: Oceans*, *129*, e2023JC020691. https://doi.org/10.1029/2023JC020691

Received 13 NOV 2023
Accepted 25 JUN 2024

Author Contributions:

Conceptualization: Kana Yamamoto, Tim DeVries, David A. Siegel, Norman B. Nelson
Data curation: Kana Yamamoto, Tim DeVries, David A. Siegel, Norman B. Nelson
Formal analysis: Kana Yamamoto
Funding acquisition: Kana Yamamoto, Tim DeVries, David A. Siegel, Norman B. Nelson
Investigation: Kana Yamamoto
Methodology: Kana Yamamoto, Tim DeVries, David A. Siegel, Norman B. Nelson

Abstract Chromophoric dissolved organic matter (CDOM) is an important part of ocean carbon biogeochemistry with relevance to long-term observations of ocean biology due to its dominant light absorption properties. Thus, understanding the underlying processes controlling CDOM distribution is important for predicting changes in light availability, primary production, and the cycling of biogeochemically important matter. We present a biogeochemical CDOM model for the open ocean with two classes of biological lability and uncertainty estimates derived from 43 ensemble members that provide a range of model parameter variations. Ensemble members were optimized to match global ocean in situ CDOM measurements and independently assessed against satellite CDOM estimates, which showed good agreement in spatial patterns. Based on the ensemble median, we estimate that about 7% of open-ocean CDOM is of terrestrial origin, but the ensemble range is large (<0.1–26%). CDOM is rapidly removed in the surface ocean (<200 m) due to biological degradation for short-lived CDOM and photodegradation for long-lived CDOM, leading to a net flux of CDOM to the surface ocean from the dark ocean. This deep-water source (ensemble median 0.001 m^{-1} yr^{-1}) is similar in magnitude to the riverine flux (0.005 m^{-1} yr^{-1}) into the surface ocean. Though discrepancies between the model and observational data remain, this work serves as a foundational framework for a mechanistic assessment of global CDOM distribution that is independent of satellite data.

Plain Language Summary The ocean holds a large pool of carbon in the form of dissolved organic matter, a complex mixture of sub-micron compounds derived from the breakdown of organisms. A subset of this mixture, called colored dissolved organic matter (CDOM), absorbs sunlight, which affects the amount of light available for photosynthesis and interferes with satellite observations of ocean biology. Thus, understanding what controls CDOM distribution in the ocean is important for predicting changes in ocean biology that affect overall carbon cycling. In this study, we present the first global ocean CDOM model that simulates CDOM distribution based on dominant production and removal mechanisms. The modeled distribution was matched to ship-based CDOM observations. Our model results show that the majority of CDOM in the open ocean is produced within the ocean rather than transported from land by rivers. CDOM is removed mainly in the surface ocean via degradation caused by light exposure, and surface CDOM is replenished by a sub-surface source. This model is broadly consistent with and independent of satellite-derived CDOM data sets, and serves as the first step in providing a mechanistic assessment of global CDOM distribution that can be used to improve satellite ocean observations.

1. Introduction

Chromophoric dissolved organic matter (CDOM) is the fraction of dissolved organic matter (DOM) that is optically active. As the dominant light-absorbing constituent of seawater in the ultraviolet to blue-green wavelengths, CDOM can regulate light availability in surface waters as well as ocean color (Fichot et al., 2023; Nelson & Siegel, 2013; Siegel et al., 2002). Thus, CDOM is an important parameter for ocean color algorithms used to quantify phytoplankton biomass (Siegel et al., 2013) that inform global estimates of the strength of the biological carbon pump (Nowicki et al., 2022; Siegel et al., 2014). However, current ocean color algorithms rely on empirical and semi-analytical relationships of CDOM optical properties rather than mechanistic models (Werdell et al., 2018). This leads to compromised estimates of chlorophyll concentrations and long-term trends due to inaccurate assessments of CDOM variability (Dutkiewicz et al., 2019; Siegel et al., 2013). Furthermore, there is rising interest in using remotely-sensed CDOM as a tracer for dissolved organic carbon (DOC) dynamics in the open ocean (Fichot et al., 2023; Iuculano et al., 2019). If possible, this would allow the use of satellites to

Supervision: Tim DeVries, David A. Siegel, Norman B. Nelson
Visualization: Kana Yamamoto
Writing – original draft: Kana Yamamoto
Writing – review & editing: Kana Yamamoto, Tim DeVries, David A. Siegel, Norman B. Nelson

indirectly observe DOC, which is largely optically inactive (Nelson & Siegel, 2013). Currently, we lack the quantitative understanding of global CDOM dynamics that is necessary to independently assess ocean color algorithms and elucidate CDOM-DOC relationships.

Unlike DOC, CDOM in the open ocean is generally depleted at the surface and increases with depth and water mass age (Catalá, Reche, Álvarez, et al., 2015; Nelson et al., 2010). This distribution arises from an interplay of external and internal sources, photochemical and biological removal mechanisms, and large-scale ocean circulation. Since the "abundance" of CDOM is measured as the light absorption at various wavelengths, typically between 300 and 450 nm, the production and removal of CDOM refer to the increase or loss of absorption at these wavelengths and do not necessarily equate to a production or removal of organic matter (more on this in Section 2.1). External sources include terrestrial inputs such as riverine discharge and coastal runoff (Cartisano et al., 2018; Del Vecchio & Subramaniam, 2004; Vodacek et al., 1997), while internal sources are attributed to the degradation of marine organic matter during heterotrophic metabolism (Catalá, Reche, Álvarez, et al., 2015; Jørgensen et al., 2011; Nelson et al., 2010; Yamashita & Tanoue, 2008). Photodegradation, or "photobleaching", at the surface is believed to be the dominant removal mechanism for CDOM (Andrews et al., 2000; Mopper et al., 1991; Swan et al., 2012). Biological processes can contribute to CDOM removal (Lønborg et al., 2010; Romera-Castillo et al., 2011), but bulk CDOM seems to be biologically recalcitrant (Catalá, Reche, Álvarez, et al., 2015; Yamashita & Tanoue, 2008) with biologically labile CDOM found mostly in the productive surface waters (Jørgensen et al., 2011; Nelson & Gauglitz, 2016; Yamashita & Tanoue, 2003). Ocean circulation connects the surface ocean waters that experience both rapid removal of CDOM by photobleaching and rapid production by microbial activity, with the deep ocean where CDOM accumulates (Kim & Kim, 2015; Nelson et al., 1998). The interactions of these mechanisms and their relative importance is yet unquantified.

In particular, the contribution of terrestrial versus marine sources of CDOM is still an active topic of research relating to the fate of terrestrial organic matter in the open ocean (Fichot et al., 2023; Kaiser et al., 2017). In coastal waters near freshwater sources, CDOM and DOC are positively correlated and covary with salinity (Del Castillo & Miller, 2008; Del Vecchio & Blough, 2004). This relationship is driven by the mixing of freshwater inputs, with high loads of CDOM and DOC and low salinity, and it allows the use of remote sensing of CDOM to study nearshore DOC dynamics (Cao et al., 2018; Fichot et al., 2023; Mannino et al., 2008). However, no such relationship exists in offshore waters (Nelson & Siegel, 2013; Siegel et al., 2002). Still, evidence of terrestrial CDOM has been observed throughout the Atlantic Ocean (Andrew et al., 2013; Jørgensen et al., 2011), particularly after high-flow discharge events from the Amazon and Orinoco Rivers (Blough et al., 1993; Del Vecchio & Subramaniam, 2004; Salisbury et al., 2011), and in the North Pacific (Cartisano et al., 2018). Furthermore, Andrew et al. (2013) and Cartisano et al. (2018) concluded that terrestrial CDOM contributes substantially to CDOM in the open ocean. However, quantitative estimates of the terrestrial contribution to bulk CDOM in the open ocean remain elusive.

In contrast, multiple studies point to a dominant contribution of microbial sources of CDOM in the open ocean. Several studies observed a strong correlation between CDOM and apparent oxygen utilization (AOU) in the Pacific and Indian Ocean, concluding that CDOM production is linked to heterotrophic degradation of organic matter (Catalá, Reche, Fuentes-Lema et al., 2015; Swan et al., 2009; Yamashita & Tanoue, 2008). Nelson et al. (2010) and Jørgensen et al. (2011) further hypothesized that CDOM is predominantly sourced from the degradation of sinking particulate organic matter (POM) based on its dominant contribution to AOU (Arístegui et al., 2002). However, no significant correlation between CDOM and AOU was found in the Atlantic Ocean, which may, in part, be obscured by the subduction of surface CDOM to depth from deep water formation in the North Atlantic (De La Fuente et al., 2014; Nelson et al., 2007).

CDOM dynamics are further complicated by the divergent removal processes controlling its dynamics. CDOM undergoes rapid removal by photobleaching as demonstrated directly by incubation experiments (Andrews et al., 2000; Stubbins & Dittmar, 2015; Swan et al., 2012) and indirectly by the depletion of CDOM at the sea surface, especially in the subtropics where insolation is high and mixed layers are shallow (Nelson et al., 1998, 2010; Nelson & Siegel, 2013). Away from the influence of sunlight, CDOM appears to be much more stable. Catalá, Reche, Álvarez, et al. (2015) estimated a CDOM lifetime for the dark ocean (depths >200 m) much higher than that of the water mass turnover time, which implies that the majority of CDOM is resistant to biological degradation. Nevertheless, studies of fluorescent DOM (FDOM), a fraction of CDOM that also fluoresces, have found evidence of more biologically labile CDOM (Jørgensen et al., 2011; Nelson & Gauglitz, 2016; Yamashita

& Tanoue, 2003), providing a microbial sink for CDOM in the deep ocean. However, FDOM optical properties suggest that biologically labile molecules decrease rapidly with depth (Jørgenson et al., 2011; Nelson & Gauglitz, 2016; Yamashita & Tanoue, 2003), potentially limiting the rate of microbial removal of CDOM in the deep ocean. The relative importance of photobleaching and microbial sinks for the global CDOM inventory has not been established.

To quantify these complex interactions, we construct a data-assimilated, global biogeochemical model of CDOM for the open ocean. We explore the following questions related to global CDOM dynamics:

1. What is the relative importance of terrestrial (riverine) versus marine (metabolic) sources of CDOM in the open ocean?
2. Is the marine source of CDOM controlled mainly by the degradation of POM or DOM?
3. What are the main removal mechanisms of CDOM in the open ocean, and how do they impact the lifetime of CDOM?
4. What is the role of large-scale ocean circulation in determining the global CDOM distribution in the open ocean?

Here, we present a two-component CDOM model with short- and long-lived CDOM for the open ocean (Section 2.2). We varied model configurations to create an ensemble of plausible models and optimized the parameters of each ensemble member to match in situ observations of CDOM in the open ocean (Section 2.3 and 2.4). Model performance was evaluated by comparing the modeled CDOM distribution to both in situ and satellite-based CDOM data sets (Section 3.1). We provide estimates of the contribution and turnover times for short-versus long-lived CDOM and terrestrial-versus marine-sourced CDOM (Section 3.2 and 3.3). We also address caveats related to both the model and the data sets we used in model optimization and evaluation (Section 4.1). Finally, we synthesize our results into a global ocean CDOM budget (Section 4.2).

2. Methods and Data

2.1. Light Absorption as a Proxy for CDOM Abundance

CDOM is operationally defined by its optical properties and consists of a diverse pool of dissolved organic compounds, the full extent of which has not been chemically described (Coble, 2007; Stedmon & Nelson, 2015). Therefore, it is not currently possible to extract the chromophoric compounds from DOM to quantify CDOM concentration in mass or carbon units. Instead, an optical property that defines the amount of light absorbed by CDOM, known as the absorption coefficient, is used as a proxy for CDOM abundance (Coble, 2007); this absorption coefficient is treated as a linearly proportional measurement of CDOM abundance (Catalá, Reche, Álvarez, et al., 2015; Nelson et al., 2007, 2010). For this paper, we use the absorption coefficient at 325 nm ($a_{CDOM}(325)$, m^{-1}) because it is the most representative measurement in the field for two reasons. First, $a_{CDOM}(325)$ has lower instrumental error than absorption coefficients in the visible wavelengths due to the exponentially decaying nature of the CDOM absorption spectra with increasing wavelength (Bricaud et al., 1981) and based on uncertainties in its measurement compared with a pure water standard (Nelson et al., 1998). Second, $a_{CDOM}(325)$ reflects the abundance of both biologically labile and refractory CDOM (Nelson et al., 1998, 2010).

2.2. Two-Component Biogeochemical CDOM Model

To quantify the biogeochemical controls of open ocean CDOM, we developed an annual climatological CDOM model. The model estimates the steady-state distribution of two CDOM pools, short- and long-lived, which represent discretized classes of biological reactivity. This is analogous to the spectrum of DOC biological lability (Hansell, 2013), but the distinction of lability for short- and long-lived pools are solely relative to each other and do not necessarily fit into the defined DOC categories of labile, semi-labile, semi-refractory, and refractory. We make this distinction between the classes of biological lability of CDOM and DOC because of the decoupled nature of CDOM and DOC and our current inability to physically identify and categorize short- and long-lived CDOM into DOC pools. The distribution of both CDOM pools in the model is driven by ocean circulation, marine sources from POC and DOC degradation, terrestrial sources from rivers, photobleaching at the sea surface, and removal via microbial degradation.

The physical transport of CDOM is simulated using a data-assimilated, global ocean circulation inverse model (OCIM). OCIM estimates the climatological mean state of the ocean circulation by fitting six circulation tracers

(potential temperature, salinity, CFC-11, CFC-12, natural radiocarbon, and natural δ^3He) and with additional model constraints of mean dynamical sea-surface topography and air-sea fluxes of heat and freshwater (DeVries, 2014, 2022; DeVries & Primeau, 2011). Here we use the latest version, OCIM2-48L, which has a horizontal resolution of 2° × 2° and 48 depth levels (Holzer et al., 2021). The surface mixed layer in the model is prescribed from annual mean observations (de Boyer Montegut et al., 2004).

The two-pool CDOM model is driven by physical transport via ocean circulation and biogeochemical sources and sinks:

$$\frac{\partial \mathrm{CDOM_{short}}}{\partial \mathrm{t}} = \mathbf{A}\mathrm{CDOM_{short}} + \mathrm{J_{source,short}} - \mathrm{J_{sink,short}} \quad (1)$$

$$\frac{\partial \mathrm{CDOM_{long}}}{\partial \mathrm{t}} = \mathbf{A}\mathrm{CDOM_{long}} + \mathrm{J_{source,long}} - \mathrm{J_{sink,long}} \quad (2)$$

where $\mathrm{CDOM_{short}}$ and $\mathrm{CDOM_{long}}$ are CDOM abundance ($\mathrm{a_{CDOM}}(325)$, $\mathrm{m^{-1}}$) for the short-lived and long-lived pools, respectively; **A** is the climatological advective-diffusive transport ($\mathrm{yr^{-1}}$) from OCIM2-48L; $\mathrm{J_{source,short}}$ and $\mathrm{J_{source,long}}$ are the biogeochemical sources ($\mathrm{m^{-1}\ yr^{-1}}$) of $\mathrm{CDOM_{short}}$ and $\mathrm{CDOM_{long}}$, respectively; and $\mathrm{J_{sink,short}}$ and $\mathrm{J_{sink,long}}$ are the biogeochemical sinks ($\mathrm{m^{-1}\ yr^{-1}}$) of $\mathrm{CDOM_{short}}$ and $\mathrm{CDOM_{long}}$, respectively. The total CDOM pool ($\mathrm{CDOM_{total}}$) is the sum of $\mathrm{CDOM_{short}}$ and $\mathrm{CDOM_{long}}$.

Modeled CDOM sources include marine sources from the degradation of POC and DOC and terrestrial sources from riverine inputs:

$$\mathrm{J_{source,short}} = \mathrm{r_{POC,short}OUR_{POC}} + \mathrm{r_{DOC,short}OUR_{DOC}} + \alpha \mathrm{F_{river}} \quad (3)$$

$$\mathrm{J_{source,long}} = \mathrm{r_{POC,long}OUR_{POC}} + \mathrm{r_{DOC,long}OUR_{DOC}} + (1-\alpha)\,\mathrm{F_{river}} \quad (4)$$

where $\mathrm{OUR_{POC}}$ and $\mathrm{OUR_{DOC}}$ are the oxygen utilization rates (mmol $\mathrm{O_2\ m^{-3}\ yr^{-1}}$) from the remineralization of bulk POC and the combined remineralization of semi-labile, semi-refractory, and refractory DOC (Figure S1 in Supporting Information S1) (Nowicki et al., 2022), respectively, as a proxy for POC and DOC degradation; $\mathrm{r_{POC,short}}$ and $\mathrm{r_{POC,long}}$ are the conversion factors ($\mathrm{m^2\ (mmol\ O_2)^{-1}}$) from the degradation of POC to $\mathrm{CDOM_{short}}$ and $\mathrm{CDOM_{long}}$, respectively; $\mathrm{r_{DOC,short}}$ and $\mathrm{r_{DOC,long}}$ are the conversion factors ($\mathrm{m^2\ (mmol\ O_2)^{-1}}$) from the degradation of DOC to $\mathrm{CDOM_{short}}$ and $\mathrm{CDOM_{long}}$, respectively; $\mathrm{F_{river}}$ is the terrestrial CDOM flux from rivers ($\mathrm{m^{-1}\ yr^{-1}}$); and α is the fraction of riverine CDOM that is short-lived. The OUR fields are from a data-assimilated biological pump model that is constrained by dissolved oxygen and DOC distribution (Nowicki et al., 2022). Within the biological pump model, the total oxygen consumption is partitioned into the respiration of discrete organic matter reservoirs (Nowicki et al., 2022). The values of $\mathrm{r_{POC,short}}$, $\mathrm{r_{POC,long}}$, $\mathrm{r_{DOC,short}}$ and $\mathrm{r_{DOC,long}}$ are adjusted to provide an optimal fit to in situ CDOM observations, and α is varied using a range of fixed values (see Section 2.3).

$\mathrm{F_{river}}$ is the product of a spatially varying freshwater flux (Kwon et al., 2021) and an estimate of the global median river $\mathrm{a_{CDOM}}(325)$ of 9 $\mathrm{m^{-1}}$. The median river $\mathrm{a_{CDOM}}(325)$ comes from over 80 in situ, river $\mathrm{a_{CDOM}}$ measurements gathered from the literature (Table S1). Only measurements taken upriver of the river mouth (salinity≤5 ppt) were included in our data set. Rivers from all seven continents except Antarctica are represented in the data set, but representation is biased toward rivers in North America ($n = 27$) and East Asia ($n = 23$). Where available, we used direct measurements of $\mathrm{a_{CDOM}}(325)$. Otherwise, the reported $\mathrm{a_{CDOM}}(\sigma)$ was converted to $\mathrm{a_{CDOM}}(325)$ from their associated spectral slope (S) using the relationship from Bricaud et al. (1981):

$$\mathrm{a_{CDOM}}(325) = \mathrm{a_{CDOM}}(\lambda)\, \mathrm{e}^{-S(325-\lambda)} \quad (5)$$

where λ is the wavelength of $\mathrm{a_{CDOM}}$ reported in the individual studies. Most studies reported S with their CDOM measurements, but for those where S was missing, a value of 0.014 $\mathrm{nm^{-1}}$ was assumed as a representative value for terrestrial, freshwater CDOM (Blough & Del Vecchio, 2002). In our river $\mathrm{a_{CDOM}}(325)$ data set, the minimum is 1.1 $\mathrm{m^{-1}}$ in the Pearl River in China (Li et al., 2019) and the maximum is 280 $\mathrm{m^{-1}}$ in the Maludam River of Malaysia (Martin et al., 2018). We chose to use the global median because the distribution of river $\mathrm{a_{CDOM}}(325)$

Table 1
Model Ensemble Members With the Adjustable and Fixed Model Parameters

Model type	$r_{POC,short}$ & $r_{POC,long}$ (m^2 (mmol O_2)$^{-1}$)	$r_{DOC,short}$ & $r_{DOC,long}$ (m^2 (mmol O_2)$^{-1}$)	$r_{bio,short}$ & $r_{bio,long}$ (yr^{-1})	r_{bleach} (yr μmol photons m^{-2} s^{-1})	α	# of models
POC + DOC	Optimized	Optimized	Optimized	3, 6.5, 10, 13.5, 17	0, 0.25, 0.5 0.75, 1	25
POC-only	Optimized	0	Optimized	3, 6.5, 10, 13.5, 17	0, 0.25, 0.5 0.75, 1	25
DOC-only	0	Optimized	Optimized	3, 6.5, 10, 13.5, 17	0, 0.25, 0.5 0.75, 1	25

was heavily right-skewed, with 10th and 90th percentiles of 3 and 100 m^{-1}. Varying the river $a_{CDOM}(325)$ regionally did not significantly affect model performance nor global accumulation of terrestrial CDOM (see Text S1 in Supporting Information S1). Thus, a constant global river $a_{CDOM}(325)$ was used to refrain from over-defining its spatial variability with limited knowledge. We test a range of α values in our models to vary the fraction of river CDOM that is long-lived; this effectively tests the sensitivity of the magnitude of river CDOM accumulation in the open ocean on model performance (see Section 2.3 and 4.2.1).

Modeled CDOM sinks include first-order removal from biological turnover and photobleaching:

$$J_{sink,short} = r_{bio,short}CDOM_{short} + \frac{PAR}{r_{bleach}}CDOM_{surf,short} \quad (6)$$

$$J_{sink,long} = r_{bio,long}CDOM_{long} + \frac{PAR}{r_{bleach}}CDOM_{surf,long} \quad (7)$$

where $r_{bio,short}$ and $r_{bio,long}$ are the specific removal rate (yr^{-1}) due to biological degradation of $CDOM_{short}$ and $CDOM_{long}$, respectively; PAR is the annual climatological photosynthetically available radiance (μmol photons m^{-2} s^{-1}) from SeaWiFS (Figure S2 in Supporting Information S1) (Siegel et al., 2014); and r_{bleach} is the PAR-dependent photobleaching timescale (yr μmol photons m^{-2} s^{-1}). The values of $r_{bio,short}$ and $r_{bio,long}$ are adjusted to provide an optimal fit to in situ CDOM observations, and r_{bleach} is varied using a range of fixed values (see Section 2.3).

2.3. Model Ensemble, Optimization, and Uncertainty

Model parameters for CDOM sources and sinks were adjusted such that the combined modeled distribution of the two CDOM pools best match in situ $a_{CDOM}(325)$ measurements. This model optimization was performed for 75 ensemble members, which are used to evaluate our model uncertainty.

We create an ensemble of models that reflect irreducible sources of uncertainty in our model. These sources of uncertainty include the bioreactivity of river CDOM (given by the value of α), the photobleaching timescale (given by the value of r_{bleach}), and the origin of marine CDOM (either POC or DOC, or a combination of both) (Table 1). In our ensemble, we test five values for α ranging from 0 to 1, where α = 0 indicates that all terrestrial CDOM from rivers is long-lived and α = 1 indicates that all terrestrial CDOM is short-lived. We also test five values for r_{bleach} which are based on published photobleaching timescales of bulk ocean CDOM from the Bermuda Atlantic Time Series (BATS) (Nelson et al., 1998) and the Mid-Atlantic Bight (Vodacek et al., 1997). Values of r_{bleach} range from 3 to 17 years μmol photons m^{-2} s^{-1}, representing global mean photobleaching timescales of roughly 35–200 days when divided by PAR. Lastly, we ran three model variations to test marine sources in which CDOM is produced as a byproduct of (a) both POC and DOC degradation, (b) only POC degradation, and (c) only DOC degradation (Table 1). Given all combinations of model configurations, the full ensemble consists of a total of 75 different models.

The values of the six other model parameters (r_{POC}, r_{DOC}, and r_{bio} for both $CDOM_{short}$ and $CDOM_{long}$) are taken as adjustable parameters, and their values are optimized so that the model best matches ship-based $a_{CDOM}(325)$ for each ensemble member (satellite data are excluded from optimization). The modeled and observed data were compared using depth-resolved region-mean values for 11 different regions: the North Pacific and North Atlantic; the northern and southern Pacific subtropics; the northern and southern Atlantic subtropics; the Indian subtropics; the Pacific, Atlantic, and Indian tropics; and the Southern Ocean (Figure S3 in Supporting Information S1). The

regions are defined by hemisphere, ocean basin, and the five biomes identified in Nowicki et al. (2022): the North Atlantic, the North Pacific, the subtropical gyres, the tropical and upwelling zones, and the Southern Ocean. Biome distinctions were based on ecosystem and physical characteristics which included primary productivity, sea surface temperature, and mixed layer depth.

The model optimum is defined by the minimum of an objective cost function:

$$\text{cost} = \frac{1}{n}\sum_{i=1}^{11}\sum_{z=1}^{48}\frac{(\bar{a}_{\text{model},i}(z) - \bar{a}_{\text{obs},i}(z))^2}{\sigma^2_{\text{obs},i}(z)} \quad (8)$$

where n is the number of depth-resolved region mean observations, $\bar{a}_{\text{model},i}(z)$ is the depth-resolved mean values of modeled $a_{CDOM}(325)$ for $CDOM_{total}$ along the tracks of the observations in region i, $\bar{a}_{\text{obs},i}(z)$ is the depth-resolved mean values of measured $a_{CDOM}(325)$ for region i, and $\sigma^2_{\text{obs},i}(z)$ is the depth-resolved spatial variance of measured $a_{CDCOM}(325)$ for region i. The minimum limit of σ^2_{obs} was set to 10^{-4} because the analytical RMSE of $a_{CDOM}(325)$ was 0.01 m^{-1} (Nelson et al., 2010).

The optimization process is initiated by an initial guess of the adjustable parameters, and the model (Equations 1–2) is solved for the steady-state distribution of $CDOM_{short}$ and $CDOM_{long}$. To get the steady-state distribution, we set Equations 1 and 2 to zero and solve the system of linear functions within a tolerance of 10^{-3} m^{-1} yr^{-1} using a generalized minimum residual method supplied with a relative residual tolerance of 10^{-6}. The optimization algorithm determines the gradient of the cost function and chooses the next set of adjustable parameter values, which gives a new modeled CDOM distribution and a new cost function value. This process is repeated until the cost function reaches a minimum, thus giving us a solution of the adjustable parameter values that result in a modeled $CDOM_{total}$ field that best matches the observations. The adjustable parameters were constrained to be >0 using a natural log transformation.

2.4. In Situ and Satellite-Based CDOM Data

The model was optimized using in situ $a_{CDOM}(325)$ measurements from the US CLIVAR hydrographic cruises from 2003 to 2010 and the AMMA cruise in 2006 (Nelson et al., 2010). These discrete measurements provide consistent, quality-controlled ocean CDOM observations along meridional transects in the Pacific, Indian, and Atlantic basins (Figure 1). To compare between modeled and observed $a_{CDOM}(325)$, the in situ measurements were re-gridded onto the OCIM2-48L grid. Then, region-mean depth profiles were calculated.

Modeled surface CDOM was also compared against satellite-based estimates of surface ocean CDOM (Swan et al., 2013), but satellite-based estimates were not included in the optimization. Satellite-based estimates were derived from the SeaWiFS GSM gridded monthly climatologies (1997–2010) of the absorption coefficient of colored detrital matter (CDM) at 443 nm ($a_{CDM}(443)$) (Siegel et al., 2013). However, CDM includes both chromophoric dissolved and POM, which have similar absorption spectral shapes. Thus, the monthly climatologies of $a_{CDM}(443)$ were converted to $a_{CDOM}(325)$ using the empirical model of Swan et al. (2013). An annual climatology of $a_{CDOM}(325)$ was constructed from the mean of the monthly climatologies to compare against our model results. The conversion model has a 20% uncertainty estimate that stems from a global generalization of the relationship between the absorption coefficients and the absorption spectra across a wide range of absorption values and ocean ecosystems (Swan et al., 2013). The conversion model was trained on open ocean data, and data points with obvious terrestrial influence from rivers were excluded in the model's development (Swan et al., 2013).

3. Results

3.1. Model Performance

3.1.1. Model Evaluation

Model performance was evaluated against observed region-mean depth profiles in 11 different regions. Region-mean depth profiles for modeled $CDOM_{total}$ and CLIVAR observations for three of these regions (North Pacific, Indian subtropics, and southern Atlantic subtropics) are shown in Figure 2 to highlight similarities and differences in performance across different sub-ensembles of the full 75-model ensemble considered here. Results for all

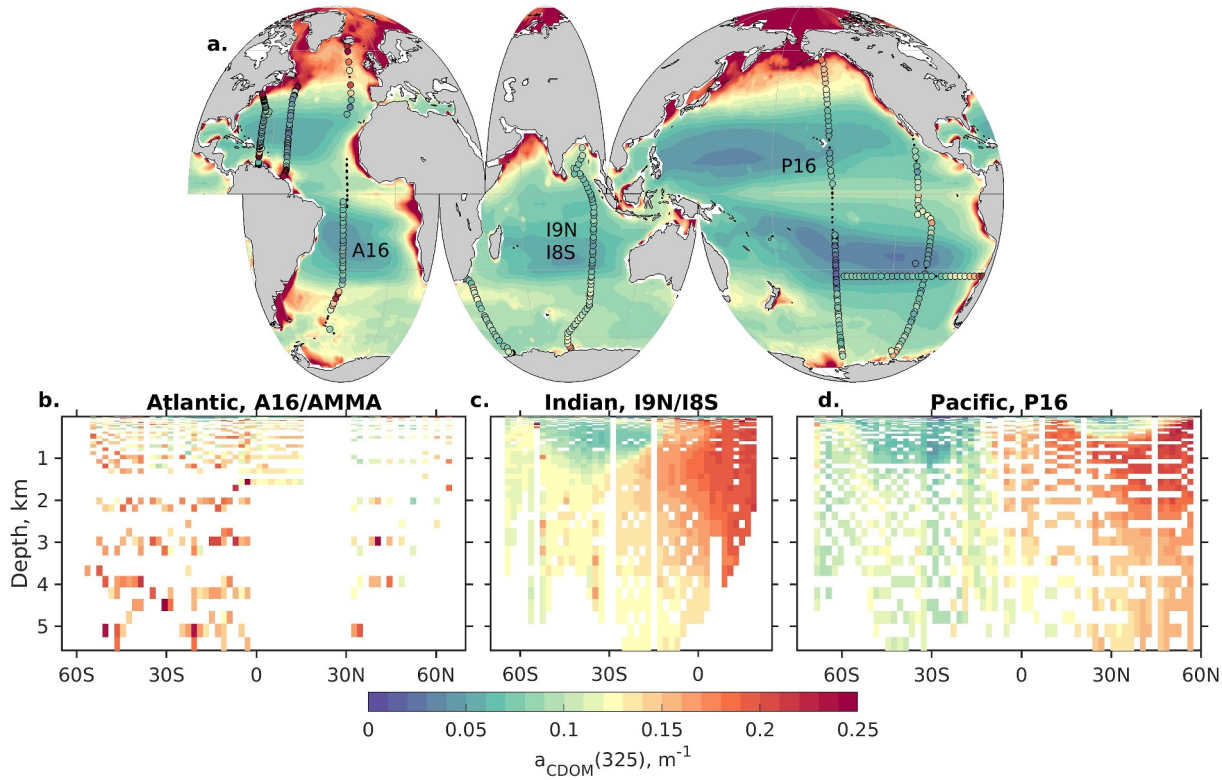

Figure 1. (a) Satellite-based estimate of surface $a_{CDOM}(325)$ with circles showing the locations of the CLIVAR and AMMA cruises. The colors of the circles show the in situ surface ($z \leq 10$ m) $a_{CDOM}(325)$ at each location. Locations where interior measurements were made but no surface data were available are shown as black dots. (b–d) Cross sections of the meridional transects in the Atlantic, Indian, and Pacific oceans from CLIVAR cruises show in situ $a_{CDOM}(325)$. The tracks of the meridional transects are labeled in panel (a).

regions are shown in Supplementary Figure S4 in Supporting Information S1. Sub-ensembles for POC + DOC and POC-only models (Table 1) can reproduce the observed region-mean depth profiles in all regions (Figures 2a–2c). These model variants perform similarly well, with model profiles falling within the observed spatial variability for each region. However, both sub-ensembles underestimate the subsurface CDOM maximum found near 100 m in the subtropics of the Indian (Figure 2b), southern Atlantic (Figure 2c), and northern Atlantic oceans (Figure S4b in Supporting Information S1). This discrepancy is discussed in more detail in Section 4.1.2. In contrast to POC + DOC and POC-only models, the DOC-only models perform poorly, generally lacking the CDOM gradient with depth seen in the observations. This is particularly evident in the North Pacific, where DOC-only models cannot reproduce the accumulation of CDOM in the oldest ocean waters between 1000 and 3,000 m (Figure 2a). The DOC-only models perform best in the Atlantic basin where observed CDOM gradients with depth are the smallest (Figure 2c and Figures S4a-c in Supporting Information S1). None of the models are able to completely match observed profiles in the southern Atlantic subtropics, particularly the high CDOM values in the deep ocean (Figure 2c).

Based on the performance of the different model types, we create a "realistic" ensemble of models that display realistic CDOM distributions. The realistic ensemble thus only includes POC + DOC and POC-only models with a cost ≤ 2 ($n = 43$). A subset of the realistic ensemble with a cost ≤ 1 ($n = 10$) is distinguished as the "best-fit" ensemble, and its performance is discussed in more detail in Section 4.1.2. Figures 2d–2f shows the mean depth profiles and spatial variability for the realistic and best-fit ensembles for the same three regions as above. The realistic ensemble members represent the full range of α values, from all terrestrial CDOM from rivers being long-lived ($\alpha = 0$) to all being short-lived ($\alpha = 1$), as well as the full range of r_{bleach} values. However, no realistic ensemble member has both an α value of 0 and the maximum photobleaching timescale. The realistic ensemble values for all model parameters are listed in Table S2 in Supporting Information S1. For the remainder of this paper, we present the realistic ensemble results and report the ensemble median and the 10th and 90th percentiles as subscripts and superscripts, respectively, to provide the ensemble estimate and uncertainty.

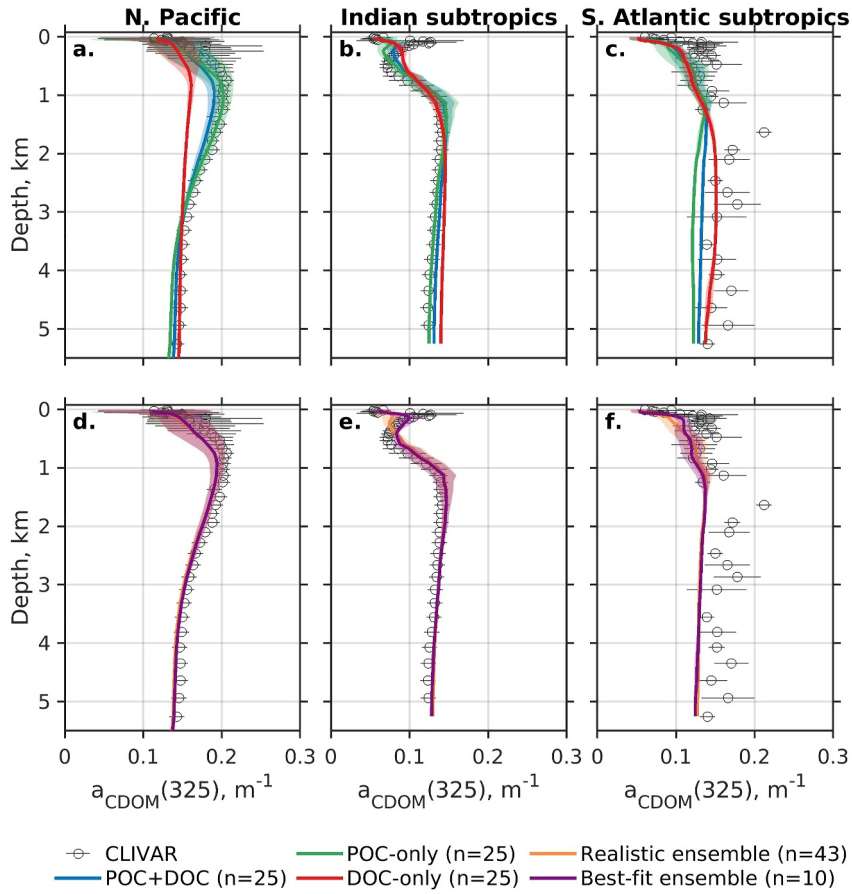

Figure 2. Region-mean depth profiles of CLIVAR CDOM observations and modeled $CDOM_{total}$ for (a–c) POC + DOC, POC-only, and DOC-only model sub-ensembles and (d–f) the realistic and best-fit ensembles. Depth profiles for all ensembles represent the ensemble mean profile. Error bars represent the spatial standard deviation of the observations, and colored shading represent the ensemble mean spatial standard deviation. Only profiles for (a, d) the North Pacific, (b, e) Indian subtropics, and (c, f) southern Atlantic subtropics are shown here, but profiles of the other 8 regions are shown in Figure S4 in Supporting Information S1.

3.1.2. Meridional Basin Cross-Sections

Mean cross-sectional transects of $CDOM_{total}$ for the realistic ensemble across the Indian, Pacific, and Atlantic basins show good fidelity to the observations in spatial trends and overall magnitude (Figures 3a–3c, see Figures 1b–1d for observations). Models replicate the accumulation of CDOM in older waters of the Indian and Pacific oceans (Figures 3a and 3b) and the depletion of CDOM in the subtropical and temperate mode waters where low-CDOM surface waters are subducted (Figures 3a–3c). The models also show elevated $a_{CDOM}(325)$ in the mid-depths (~500–3,000 m) of the Atlantic (Figure 3c) where recently subducted Antarctic intermediate waters carry CDOM-rich water. The Atlantic basin has the lowest $a_{CDOM}(325)$ due to the mixing of low-CDOM surface waters from the formation of the North Atlantic Deep Water (Figure 3c). The ensemble global mean $a_{CDOM}(325)$ is $0.14^{0.14}_{0.14}$ m^{-1} for the realistic ensemble, which matches the observed global mean $a_{CDOM}(325)$ of 0.14 m^{-1}. However, the ensemble spatial variability for the realistic ensemble, measured using the standard deviation, is lower ($0.025^{0.031}_{0.021}$ m^{-1}) compared to the observed spatial variability (0.032 m^{-1}). This is because the intra-basin contrast of low and high CDOM waters is less pronounced in the models than in the observations.

Ensemble mean cross-sectional transects of the difference between the modeled $CDOM_{total}$ and the observation show distinct model biases (Figures 3d–3f). The models generally underestimate $a_{CDOM}(325)$ in the northern Indian and Pacific deep waters and overestimate $a_{CDOM}(325)$ in the southern Indian and Pacific intermediate and deep waters (Figures 3d and 3e). This pattern seems to be reversed in the Atlantic where the models underestimate $a_{CDOM}(325)$ in the southern Atlantic Ocean (Figure 3f), but the relative scarcity of observations in the North

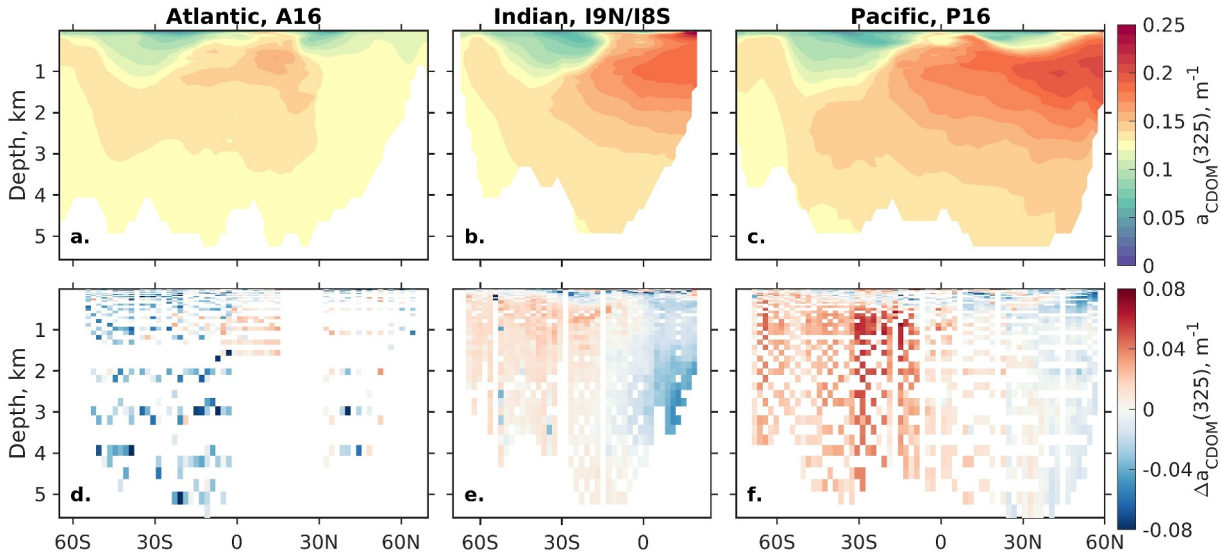

Figure 3. Ensemble mean meridional cross-sections of (a–c) modeled $CDOM_{total}$ for the realistic ensemble and (d–f) the difference between modeled and observed CDOM along (a, d) ~30°W in the Atlantic (CLIVAR transects A16N/S and AMMA transect), (b, e) ~90°E in the Indian (CLIVAR transects I9N/I8S), and (c, f) ~150°W in the Pacific (CLIVAR transects P16N/S). Red (blue) hues in panels (d–f) indicate that modeled $a_{CDOM}(325)$ is higher (lower) than the observations. Percent error plots are shown in Figure S5 in Supporting Information S1.

Atlantic makes drawing comparisons here difficult (Figure 1d). For the realistic ensemble, the global mean absolute error (MAE) is $0.017^{0.018}_{0.015}$ m^{-1}, or an observation-normalized error of 14^{15}_{12}%. Overall, the models reproduce the observed gradient of CDOM from younger to older waters, but the models accumulate slightly less CDOM in older waters and have more CDOM in younger waters compared to observations.

3.1.3. Surface CDOM

A comparison between modeled $CDOM_{total}$ and satellite-based surface $a_{CDOM}(325)$ also shows general agreement in global spatial trends (Figure 4, see Figure 1a for satellite data set), even though the satellite data set was not included in the model optimization. The models produce global minima in the subtropical gyres where photobleaching rates are high and local maxima in tropical regions where CDOM-rich waters are upwelled (Figure 4a). $a_{CDOM}(325)$ is generally high along continental margins due to outflows of CDOM-rich rivers, but the distribution of $a_{CDOM}(325)$ along the continental margins is patchier in the models (Figure 4a) than in satellite-based estimates (Figure 1a). This is more evident in the difference map between model and satellite-based estimates (Figure 4b). For example, the models overestimate $a_{CDOM}(325)$ near the Amazon and Orinoco River mouths compared to the satellite-based estimates but underestimate $a_{CDOM}(325)$ along coastlines that are less impacted by heavy river outflows (Figure 4b). Modeled $CDOM_{total}$ is also lower in the high latitudes above 45°N and below 60°S compared to the satellite-based estimates (Figure 4b). Overall, the MAE is $0.038^{0.042}_{0.035}$ m^{-1} (satellite-normalized error of 29^{34}_{27}%) with positive model biases in the low latitudes and negative model biases in the high latitudes compared to the satellite-based climatology.

Patterns of model bias are similar when compared against CLIVAR surface data ($z \leq 10$ m) where available, plotted as circles on Figure 4. As with satellite-based estimates, much of the model bias is along continental margins and high latitudes. Although CLIVAR data availability is sparse in these regions, the model similarly overestimates near the Amazon and Orinoco River mouths and underestimates in the North Atlantic (Figure 4b). The MAE with respect to CLIVAR surface data is $0.038^{0.045}_{0.037}$ m^{-1}, or an observation-normalized error of 51^{63}_{41}%. In comparison, the MAE between CLIVAR surface and satellite data is slightly lower at 0.030 m^{-1}, or an observation-normalized error of 37%. It is important to note, however, that there are caveats to both the model and satellite-based estimates of $a_{CDOM}(325)$, as well as sampling biases in the CLIVAR observations, that may result in the model differences outlined in Section 3.1.2 and 3.1.3. We discuss these caveats in more detail in Section 4.1.

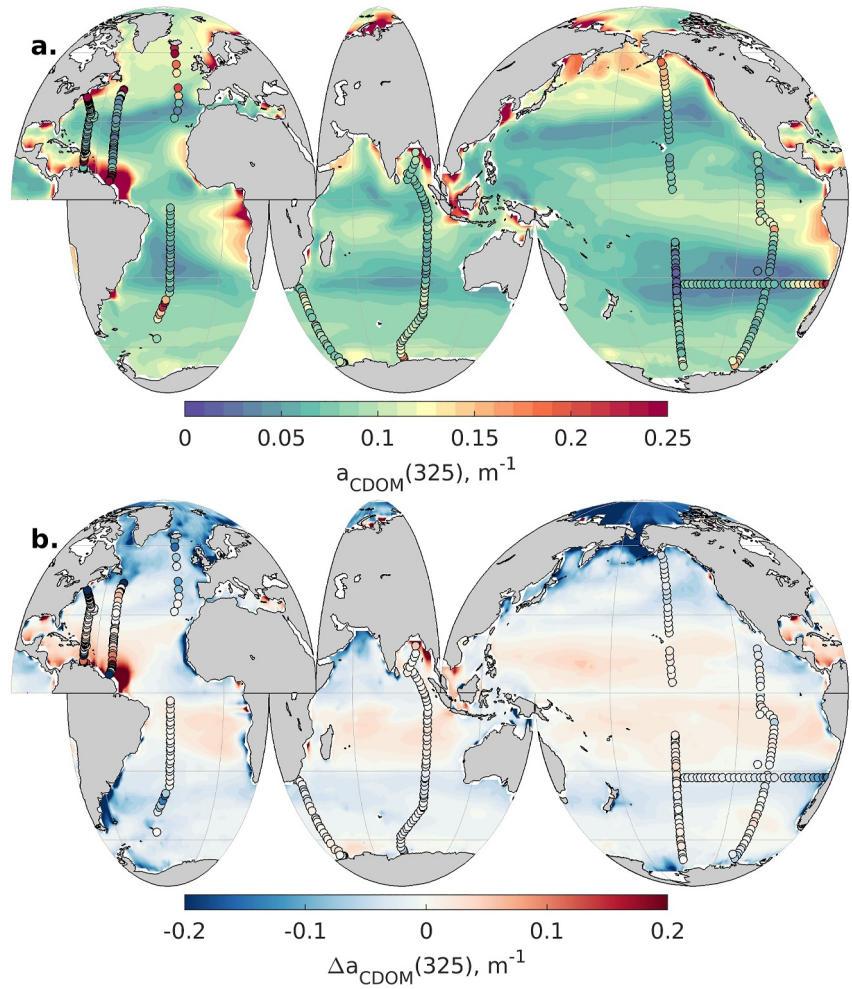

Figure 4. Ensemble mean surface map of (a) modeled $CDOM_{total}$ for the realistic ensemble with CLIVAR surface ($z \leq 10$ m) $a_{CDOM}(325)$ measurements shown in circles, and (b) the difference between modeled $CDOM_{total}$ and satellite-based surface $a_{CDOM}(325)$ with the difference between the modeled $CDOM_{total}$ and CLIVAR surface $a_{CDOM}(325)$ overlaid in circles. Red (blue) hues in panel (b) indicate that modeled $a_{CDOM}(325)$ is higher (lower) than the satellite-based and CLIVAR $a_{CDOM}(325)$. Percent error map is shown in Figure S6 in Supporting Information S1.

3.2. Distribution and Lifetimes of Short- and Long-Lived CDOM

$CDOM_{short}$ abundance is generally uniform across the global surface ocean with an increase along continental margins (not shown), but the relative contribution of $CDOM_{short}$ in surface waters varies with region (Figure 5a) due to the spatial variability of $CDOM_{long}$. In the surface ocean, $CDOM_{short}$ contributes as much as ~40% of the bulk CDOM in the tropics and subtropics where $CDOM_{long}$ is depleted (Figure 5a). This ratio decreases in coastal upwelling zones along the eastern boundaries of the Pacific and Atlantic and in higher latitudes (Figure 5a), where more $CDOM_{long}$ accumulates due to upwelling of $CDOM_{long}$-rich deep waters, and due to slower photo-degradation of $CDOM_{long}$ at high latitudes. Globally, $CDOM_{short}$ is only $0.7^{2.4}_{0.0}$% of bulk CDOM. The ratio of $CDOM_{short}$ to bulk CDOM is highest at the surface, with a global mean value of $18^{43}_{1.0}$%, and quickly declines to near zero below 1000 m (Figure 5b).

The lifetime for the short-lived CDOM pool in the global ocean is $0.77^{3.29}_{0.01}$ yr for the realistic ensemble. In comparison, the lifetime of the long-lived pool is 190^{280}_{130} yr. The short lifetime and a nonzero abundance of $CDOM_{short}$ decreases the bulk CDOM lifetime compared to that of $CDOM_{long}$ to 57^{120}_{27} yr.

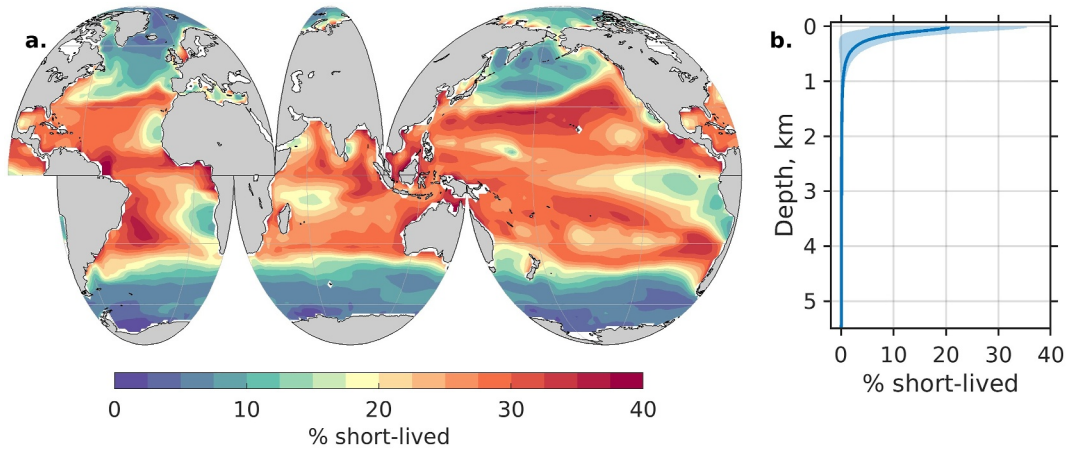

Figure 5. Relative contribution of short-lived CDOM (a) at the surface and (b) at depth in the realistic ensemble. The depth profile in panel (b) shows the ensemble mean with shading indicating the ensemble standard deviation.

3.3. Contribution of Terrestrial CDOM

The percent of open ocean CDOM that is of terrestrial origin is highest at the surface where rivers enter the ocean, decreases rapidly with depth, and then increases slightly below ~500 m, maintaining a roughly uniform contribution below 2000 m (Figure 6a). Globally, terrestrial-sourced CDOM is only $6.9^{18.6}_{0.1}$% of bulk CDOM in the open ocean in the realistic ensemble, thus making the majority of open ocean CDOM of marine origin. However, with a ratio of $10.7^{26.2}_{0.2}$%, the contribution of terrestrial CDOM tends to be higher in the Atlantic than in other oceans. This is illustrated in Figure 6a where the mean ratio of terrestrial-sourced to total CDOM in the deep Atlantic is consistently higher than that for the global ocean. This is in line with the fact that 45% of the global riverine CDOM enters the Atlantic basin.

The fraction of terrestrial CDOM in the global ocean varies with the fixed values of α and r_{bleach} in our model (Figure 6b). The terrestrial CDOM fraction decreases as α increases (Figure 6b) because higher α values indicate a higher fraction of short-lived CDOM in riverine CDOM; this fraction of riverine CDOM degrades rapidly

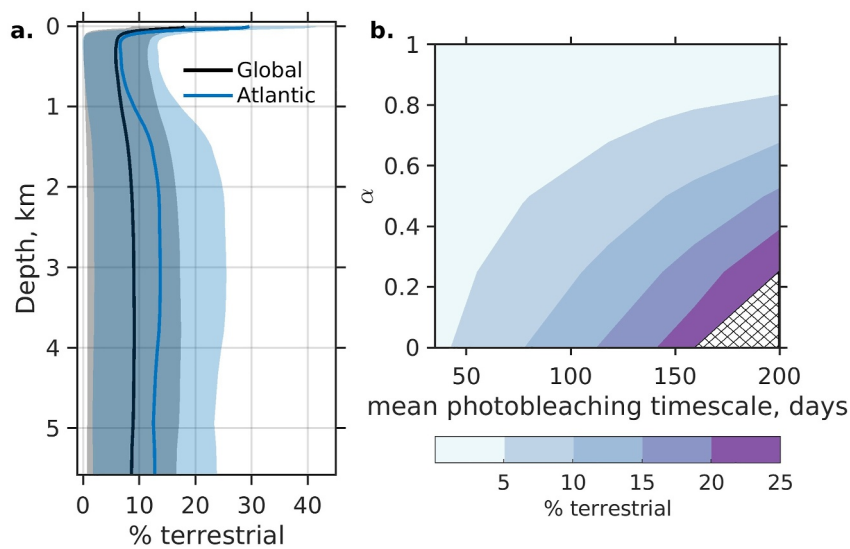

Figure 6. (a) Ensemble mean depth profiles of the terrestrial CDOM contribution for the global ocean and the Atlantic for the realistic ensemble. Shading shows the ensemble standard deviation. (b) Contour plot of terrestrial contribution as a function of the fixed variables, the global mean photobleaching timescale in days ($365*r_{bleach}/PAR$) and the fraction of $CDOM_{short}$ in riverine CDOM (α). Hatching in panel (b) indicates a lack of data because models with a global mean photobleaching timescale of 200 days and an α of 0 did not make it into the realistic ensemble.

resulting in a lower accumulation of terrestrial CDOM. The fraction of terrestrial CDOM also decreases as the photobleaching timescale decreases (Figure 6b). Lower r_{bleach} values indicate a higher photochemical removal rate at the surface, which reduces the accumulation of riverine CDOM that enters at the sea surface.

4. Discussion

In the following, we address the caveats associated with our results with respect to both our biogeochemical model and the data sets we used to optimize and assess model performance. We then present model estimates of the global CDOM budget and break down our analysis for terrestrial sources from rivers, marine sources from POC and DOC, photochemical and biological sinks, and the role of circulation.

4.1. Caveats

Disagreements between this model and the CDOM data sets detailed in Section 3.1 point to weaknesses of the model as well as known issues of the data sets themselves. We first discuss the weaknesses and caveats of the numerical model. We then explore the problems in the in situ measurements that were used for model optimization and the independent, satellite-based surface CDOM estimates that were used for secondary model evaluation.

4.1.1. Caveats of the Model

Although modeled CDOM concentrations are in general agreement with observations, important caveats remain. First, this model does not resolve seasonal or interannual variability in CDOM sources or sinks, which are known to be significant. Terrestrial CDOM from river outflows follow seasonal patterns of rainfall (Salisbury et al., 2011; Spencer et al., 2008) and exhibit interannual variability related to anomalous drought and storm events. Marine CDOM production is often tied to biological activity and thus can exhibit similar seasonal phases, with peak CDOM production occurring after large phytoplankton blooms (Allen et al., 2020; Hu et al., 2006). A time-series study at BATS also indicates seasonal variability in photodegradation rates driven by seasonality in solar radiation and mixed layer depth (Nelson et al., 1998), which is not represented in the model. Similarly, the physical mixing of CDOM between the surface and deep ocean is subject to seasonal deep-water formation and upwelling that is not represented by the climatological mean-state circulation model used here. How such temporal variability in CDOM sources, sinks, and circulation will impact global CDOM dynamics is yet undetermined. Assessing the impact of these interactions on open-ocean CDOM will require a model that resolves seasonal and interannual variability in ocean circulation and biogeochemistry, which is outside the scope of this paper.

Second, the model does not represent all potential processes affecting CDOM cycling in the global ocean. One key simplification of our model is the lack of coastal or shelf processes. Given the coarse horizontal resolution of the model grid ($2° \times 2°$), we limit our analysis to the open ocean. Therefore, we do not include nearshore processes such as the flocculation of CDOM as freshwater is mixed with seawater (Asmala et al., 2014; Maie et al., 2008); and benthic sources from pore waters (Yamashita et al., 2020; Yang et al., 2014) and sediment resuspension (Boss et al., 2001). Presumably, the inclusion of flocculation at the land-sea interface would lead to rapid removal of river CDOM, resulting in less accumulation of riverine CDOM. The lack of coastal and shelf benthic sources may explain why the modeled surface CDOM along continental margins are generally lower (away from major river mouths) than satellite-based CDOM estimates (Figure 4). Other mechanisms that are not explicitly modeled include the increased production of CDOM under hypoxic conditions (Kim & Kim, 2016; Margolin et al., 2018) and CDOM production from viral lysis (Chen et al., 2022; Zhao et al., 2017). These would not be reflected in our parameterization of CDOM production being tied to oxygen consumption, though they would partially offset the optimized biological loss rate of CDOM (r_{bio}). Explicitly including these sources may resolve the model's underestimation of CDOM accumulation in the older waters of the Indian and Pacific Ocean (Figure 3). Direct autotrophic CDOM production from phytoplankton has also been observed (Barrón et al., 2014; Romera-Castillo et al., 2010; Steinberg et al., 2004), but this production pathway cannot be distinguished using our net OUR data set. Nevertheless, on global scales, CDOM production via heterotrophic metabolism is the primary CDOM source in the open ocean (Figure 2 and Section 3.1.1).

4.1.2. Caveats of In Situ and Satellite Observations

In situ CDOM measurements are subject to sampling limitations that result in poor temporal and geographic coverage. The issue arising from poor temporal coverage is best illustrated by the best-fit ensemble, a subset of the realistic ensemble that most closely fits the observed CDOM depth profiles (Figures 2d–2f). The best-fit ensemble matches the magnitude of the subsurface CDOM maximum in the Indian and southern Atlantic subtropics (Figures 2e and 2f) better than the realistic ensemble. However, the elevated subsurface CDOM maximum in the subtropics is highly seasonal; the shallowing of the mixed layer in the summers leads to increased accumulation of CDOM below the mixed layer (Nelson et al., 1998). Due to ship sampling logistics, CDOM measurements in the South Atlantic and Indian subtropics were primarily taken during the Southern hemisphere summer/early fall (February and March, respectively), and repeat measurements at additional seasons have yet to be taken. Furthermore, the photobleaching timescale of $0.15^{0.21}_{0.10}$ yr for the best-fit ensemble is shorter compared to $0.32^{0.55}_{0.10}$ yr of the realistic ensemble, which is consistent with faster photobleaching rates during summer or fair-weather conditions. This suggests that the observations, and in turn the best-fit ensemble, are biased toward summer-like conditions rather than a true climatological state.

In situ measurements are also geographically limited. For example, CLIVAR observations above 60°N are almost completely lacking (Figure 1a). This limits model validation in the northern high latitudes where polar-specific processes such as CDOM-sea ice interactions (Huang et al., 2022; Stedmon et al., 2007) are not captured by our model or observations. The Arctic also exhibits an exceptionally large influence of terrestrial organic matter flux relative to other ocean basins (Dittmar & Kattner, 2003), reflecting an important observational gap in diagnosing the contribution of terrestrial CDOM. Some observations in the Arctic do exist. An Arctic CDOM data set compiled by Matsuoka et al. (2014) has a median $a_{CDOM}(443)$ of 0.058 m^{-1}, which corresponds to $a_{CDOM}(325)$ of 0.50 m^{-1} given their reported spectral slope. This is much higher than our estimate of surface $a_{CDOM}(325)$ in the Arctic region, with a value of $0.14^{0.24}_{0.10}$ m^{-1} for the realistic ensemble, but their Arctic data set is limited to shelf regions where higher CDOM is expected than in offshore waters. Another region with less coverage relative to other basins is the Atlantic. And in fact, none of the members in the realistic ensemble perform well in the South Atlantic subtropics (Figures 2c and f) where quality control of the data was difficult due to noise introduced from sampling discrepancies during the CLIVAR A16S cruise (Nelson and Swan, unpublished data).

Satellite observations also have limited coverage in the high latitudes during hemispheric winters. Though we performed a simple gap-filling procedure for the monthly satellite climatologies before determining annual mean values, the annual mean are still likely biased toward summer values. Thus, elevated concentrations of surface CDOM shown in the satellite-based data set may be skewed toward peak riverine CDOM flux from summer discharge flow (Clark et al., 2022; Huang et al., 2022). This could in part explain why our model estimate of CDOM is lower in the Arctic compared to satellite-based estimates (Figure 4b). Further, satellite-based estimates are also based on optical and empirical models (Garver & Siegel, 1997; Maritorena et al., 2002; Swan et al., 2013) that may not be well calibrated to the high latitudes where in situ observations are limited and terrestrial sources are higher. Although Ortega-Retuerta et al. (2010) found good agreement between remote-sensing and in situ $a_{CDM}(443)$ near the Antarctic Peninsula, they also found that detrital particles contributed more to CDM than at lower latitudes, which they attributed to snow and glacial melt. Such terrestrial influence could lead to errors in the estimation of $a_{CDOM}(325)$ from $a_{CDM}(443)$ using the Swan et al. (2013) model.

Thus, there is much room for improvement in both the biogeochemical model and the observational data sets used. Nevertheless, we present our model as the necessary first step in providing estimates for the global CDOM budget.

4.2. CDOM Sources and Sinks

The model results presented here enable us to construct a bulk CDOM ($CDOM_{total}$) budget for the open ocean, partitioned into the surface (0–200 m) and the dark ocean (>200 m) (Figure 7). Bulk CDOM increases with depth with a mean $a_{CDOM}(325)$ of $0.11^{0.12}_{0.10}$ m^{-1} in the surface ocean compared to $0.14^{0.14}_{0.13}$ m^{-1} at depth. In the surface ocean, CDOM sources include marine heterotrophic production and riverine inputs; marine sources ($0.04^{0.08}_{0.02}$ m^{-1} yr^{-1}) are higher than riverine inputs (0.005 m^{-1} yr^{-1}) by 8-fold. CDOM sinks include photobleaching and biological degradation; removal by biological degradation is slightly higher at $-0.03^{-0.00}_{-0.23}$ m^{-1} yr^{-1} than photobleaching at $-0.02^{-0.01}_{-0.06}$ m^{-1} yr^{-1}. Total removal is higher than the combined CDOM sources in the surface

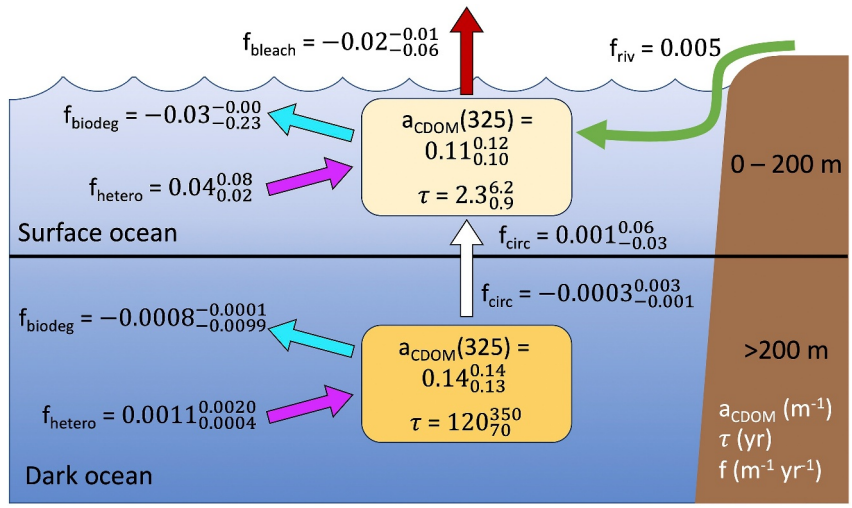

Figure 7. Global budget for $CDOM_{total}$ with rates of heterotrophic production (f_{hetero}), riverine input (f_{riv}), biological degradation (f_{biodeg}), and photobleaching (f_{bleach}) for the surface ocean (0–200 m) and the dark ocean (>200 m). Ocean circulation leads to a net exchange of CDOM between the two depth layers (f_{circ}). All rate fluxes are in units of m^{-1} yr^{-1}, normalized to the respective volume of the ocean layer. Mean $a_{CDOM}(325)$ (m^{-1}) for each layer is given inside the yellow rectangles and the lifetime of $CDOM_{total}$ (τ, yr) for each layer is also shown. All values provided are the realistic ensemble median with the subscripts and superscripts noting the 10th and 90th percentiles, respectively.

ocean, so there is a net flux of CDOM into the surface ocean from the dark ocean amounting to $0.001^{0.02}_{-0.05}$ m^{-1} yr^{-1}, which is similar to the riverine flux into the surface ocean. The $CDOM_{total}$ lifetime in the surface ocean is $2.3^{6.2}_{0.9}$ yr.

In the dark ocean, heterotrophic production and biological degradation are the sole source and sink in the model, respectively (Figure 7). Heterotrophic production ($0.0011^{0.0020}_{0.0004}$ m^{-1} yr^{-1}) outpaces biological degradation ($-0.0008^{-0.0001}_{-0.0099}$ m^{-1} yr^{-1}), leading to a flux out of the dark ocean into the surface ocean of $-0.0003^{0.003}_{-0.001}$ m^{-1} yr^{-1}. This flux out of the dark ocean is equivalent to the flux into the surface ocean after accounting for the difference in volumes between the two layers, which varies by a factor of 18. The $CDOM_{total}$ lifetime in the dark ocean is much longer at 120^{350}_{70} yr than that in the surface ocean.

Our estimate of $CDOM_{total}$ lifetime is shorter than that estimated by Catalá, Reche, Álvarez, et al. (2015). Based on water mass type analysis of AOU and $a_{CDOM}(325)$, they estimated a turnover time of 634 ± 120 years in the dark ocean. However, their study only covers a latitude range of 30°N-40°S which excludes younger water masses formed in the high latitudes. Since younger waters have a higher contribution of $CDOM_{short}$ subducted to depth, this decreases the turnover time of bulk CDOM. Their estimate is likely more comparable to our estimate of $CDOM_{long}$ lifetime in the dark ocean, which is 700^{1000}_{450} yr. This lifetime is slightly higher, though within the uncertainty, than the lifetimes of 435 ± 41 and 610 ± 55 years that Catalá, Reche, Fuentes-Lema et al. (2015) found for two different humic-like FDOM fractions. Because not all CDOM fluoresces (Stedmon & Nelson, 2015), some discrepancy in lifetime estimates between our work and Catalá, Reche, Fuentes-Lema et al. (2015) is to be expected.

4.2.1. Terrestrial Versus Marine-Sourced CDOM

Open ocean CDOM is predominantly of marine origin, with an estimated 6.9% being of terrestrial origin, but our ensemble shows a substantial range of terrestrial contributions from <0.1% to 26%. Within our ensemble, we tested the full range of α values to vary the biological lability of terrestrial CDOM which allowed for a variable accumulation of terrestrial CDOM in the open ocean. This also acted as a sensitivity test for the magnitude of riverine CDOM flux on the global CDOM distribution. We found that model performance was not sensitive to the accumulation of terrestrial CDOM; the member with the lowest terrestrial CDOM contribution performed similarly to the member with the highest contribution. We may also consider $\alpha = 1$ (all short-lived) to be unrealistic due to observed biomarkers of terrestrial CDOM in the deep ocean (Cartisano et al., 2018; Jørgensen

et al., 2011; Meyers-Schulte & Hedges, 1986; Opsahl & Benner, 1997), which speaks to some fraction of terrestrial CDOM being long-lived. In excluding realistic ensemble members with $\alpha = 1$, the updated terrestrial contribution estimate is only slightly higher ($7.6^{24.1}_{2.1}$%). Our inverse model simulations imply that riverine sources do not play a dominant role in controlling open ocean CDOM. This in line with studies that have suggested the main source to be from marine heterotrophic production based on observed inverse relationships between CDOM and AOU (Catalá, Reche, Álvarez, et al., 2015; Jørgensen et al., 2011; Nelson et al., 2010; Yamashita & Tanoue, 2008). However, the wide range of modeled terrestrial CDOM fractions that are consistent with open-ocean CDOM observations points to the need for better constraints on the total flux of terrestrial CDOM and how it is processed across the land-ocean aquatic continuum.

Equivalent estimates of the contribution of terrestrial-sourced CDOM to bulk CDOM in the open ocean do not exist in the literature. However, we can compare our estimates to previous studies on subfractions of CDOM. To our knowledge, the only quantitative estimate of terrestrial-sourced CDOM fractions comes from the very first estimate of terrestrial-derived humic substances in the equatorial Pacific provided by Meyers-Schulte and Hedges (1986). Based on the isolation of lignin-derived phenols within humic isolates, they estimated that roughly 10% of the sampled humic substance is of terrestrial origin. However, bulk CDOM is not limited to humic substances nor are all humic substances colored (Coble, 2007), so their estimates are not directly comparable to ours; still, they are of similar magnitude. In contrast, based on fluorescence characteristics of CDOM, Andrew et al. (2013) concluded that a "major" terrestrial component of CDOM is present in the Equatorial Atlantic, and Cartisano et al. (2018) noted a "substantial" terrigenous component of humic-like CDOM in the North Pacific. Such fluorescence studies confirm the ubiquity of terrestrial CDOM in the global ocean but only provide qualitative determinations. Furthermore, this conclusion was largely based on an analysis of extracted CDOM, which did not yield 100% extraction from the original samples. Their extraction method was especially poor in the UV absorption band, with the extracted samples having only ~40% of the absorption observed in the original samples at 325 nm (Cartisano et al., 2018). Cartisano et al. (2018) also noted a strong correlation between lignin-derived phenol concentrations and $a_{CDOM}(285)$ and $a_{CDOM}(350)$ in support of their conclusion. However, our estimates, which are consistent with observed bulk CDOM distributions, indicate a relatively low terrestrial influence on open-ocean CDOM.

4.2.2. Heterotrophic CDOM Production From POC Versus DOC Degradation

We further break down marine-sourced CDOM into that derived from POC and DOC. Based on 24 members of the realistic ensemble that include CDOM sources from both POC and DOC degradation, 79^{98}_{43}% of the marine-sourced CDOM that accumulates in the open ocean comes from POC degradation, and 21^{57}_{2}% comes from DOC degradation. This is consistent with the contribution of POC remineralization to AOU of roughly 90% in the global ocean (Arístegui et al., 2002). Our estimate supports the hypothesis from Nelson et al. (2010) and Jørgenson et al. (2011) that CDOM in the open ocean is marine-sourced and predominantly a by-product of the heterotrophic degradation of POC.

4.2.3. CDOM Removal Mechanisms

This model includes two removal mechanisms: biological degradation and photobleaching. For the more biologically reactive $CDOM_{short}$, the turnover time due to biological degradation is $0.5^{2.4}_{0.01}$ yr for the whole ocean. For $CDOM_{long}$, it is 8000^{11000}_{4600} yr, making this pool incredibly resistant to biological degradation. Comparatively, the turnover time due to photobleaching is $5.4^{17.7}_{0.3}$ yr and 180^{320}_{50} yr for the short- and long-lived pools, respectively. Thus, removal due to biological degradation controls $CDOM_{short}$, while photobleaching dominates for $CDOM_{long}$. This is also reflected in the vertical profiles of each pool. $CDOM_{short}$ is highest at the surface and decreases rapidly with depth (Figure S7 in Supporting Information S1) because it is controlled by biological activity which is highest at the surface. This profile is consistent with observed profiles of amino acid-like FDOM decreasing with depth to ~500 m and remaining low below 500 m (Jørgenson et al., 2011; Nelson & Gauglitz, 2016). In contrast, $CDOM_{long}$ is depleted at the surface where photobleaching occurs and generally increases with depth, though depth profiles vary based on water mass mixing and CDOM accumulation (Figure S7 in Supporting Information S1). Since $CDOM_{short}$ accounts for less than 1% of $CDOM_{total}$ globally, photobleaching acts as the first-order control of CDOM removal in the open ocean.

4.2.4. The Role of Ocean Circulation

The estimated source of $CDOM_{total}$ into the surface ocean from the dark ocean (0.001 m^{-1} yr^{-1}) is on the same order as the riverine source (0.005 m^{-1} yr^{-1}). However, the net transport of $CDOM_{total}$ across the two layers for the realistic ensemble ranges from being a source to a sink in the surface ocean. This wide range is driven by the transport of $CDOM_{short}$. While the estimated net transport of $CDOM_{long}$ is consistently positive into the surface ocean across the realistic ensemble members ($0.004^{0.030}_{0.001}$ m^{-1} yr^{-1}), the net transport of $CDOM_{short}$ is highly variable with an ensemble estimate of $-0.001^{0.09}_{-0.02}$ m^{-1} yr^{-1}. Thus, we can be confident that $CDOM_{long}$ in the surface ocean is supplied from the dark ocean, but there is still some uncertainty on the effect of circulation on $CDOM_{short}$ due to uncertainty in the $CDOM_{short}$ depth profile (Figure S7 in Supporting Information S1).

5. Conclusions

We present the first global CDOM budget quantified using a data-assimilated biogeochemical model that resolves two classes of CDOM based on biological lability. Based on the model ensemble median, we estimate that about 7% of open ocean CDOM is of terrestrial origin and that the primary source of CDOM is from the heterotrophic degradation of POC (~80%). Bulk CDOM is almost entirely long-lived (~99% of global $CDOM_{total}$), which is highly biologically recalcitrant but photochemically labile. However, photobleaching is limited to the sunlit surface, making the removal of CDOM limited by ocean overturning. The model reproduces the in situ CDOM measurements across the global ocean, but some deviations are present. These point to important weaknesses relating to both the model construction and observational biases, including lack of seasonal variability in the model, the seasonal bias of both in situ measurements and satellite-based surface CDOM estimates, and poor representation of polar processes across all three data sets. Future steps should include developing a seasonal CDOM model and incorporating in situ measurements from the high latitudes, especially from the Arctic Ocean. This work establishes a foundational framework that can be built upon to create an independent, mechanistic assessment of CDOM, which could aid in the separation of CDOM and chlorophyll from satellite ocean color data in the future.

Data Availability Statement

Data used for this work are available in the following references. Oxygen utilization rate data from Nowicki et al. (2022). Riverine freshwater flux data from Kwon et al. (2021). Photosynthetically available radiance data from Siegel et al. (2014). OCIM2-48L model output from Holzer et al. (2021). In situ CDOM measurements from the US CLIVAR hydrographic cruises are available on SeaBASS (Carlson et al., 1999). SeaWiFS GSM CDM monthly climatologies are available on NASA OB. DAAC (NASA, 2022). Model inputs, outputs, and scripts to run the CDOM model and plot the figures are available on a public repository (https://doi.org/10.5281/zenodo.10884299).

Acknowledgments
KY acknowledges support from Future Investigators in NASA Earth and Space Science and Technology (FINESST) Award 80NSSC21K1625. TD acknowledges support from the National Science Foundation under Grant 2049509. DAS acknowledges support from NASA Grants 80NSSC17K0692 and 80NSSC20M0226. The authors have no conflicts of interest relevant to this study.

References

Allen, J. G., Siegel, D. A., Nelson, N. B., & Halewood, S. (2020). Controls on ocean color spectra observed during the North Atlantic Aerosols and Marine Ecosystems Study (NAAMES). *Frontiers in Marine Science*, *7*, 567007. https://doi.org/10.3389/fmars.2020.567007

Andrew, A. A., Del Vecchio, R., Subramaniam, A., & Blough, N. V. (2013). Chromophoric dissolved organic matter (CDOM) in the equatorial Atlantic Ocean: Optical properties and their relation to CDOM structure and source. *Marine Chemistry*, *148*, 33–43. https://doi.org/10.1016/j.marchem.2012.11.001

Andrews, S. S., Caron, S., & Zafiriou, O. C. (2000). Photochemical oxygen consumption in marine waters: A major sink for colored dissolved organic matter? *Limnology & Oceanography*, *45*(2), 267–277. https://doi.org/10.4319/lo.2000.45.2.0267

Arístegui, J., Duarte, C. M., Agustí, S., Doval, M., Álvarez-Salgado, X. A., & Hansell, D. A. (2002). Dissolved organic carbon support of respiration in the dark ocean. *Science*, *298*(5600), 1967. https://doi.org/10.1126/science.1076746

Asmala, E., Bowers, D. G., Autio, R., Kaartokallio, H., & Thomas, D. N. (2014). Qualitative changes of riverine dissolved organic matter at low salinities due to flocculation. *Journal of Geophysical Research: Biogeosciences*, *119*(10), 1919–1933. https://doi.org/10.1002/2014JG002722

Barrón, R. K., Siegel, D. A., & Guillocheau, N. (2014). Evaluating the importance of phytoplankton community structure to the optical properties of the Santa Barbara channel, California. *Limnology & Oceanography*, *59*(3), 927–946. https://doi.org/10.4319/lo.2014.59.3.0927

Blough, N. V., & Del Vecchio, R. (2002). Chromophoric DOM in the coastal environment. In D. A. Hansell & C. A. Carlson (Eds.), *Biogeochemistry of marine dissolved organic matter* (pp. 509–546). Academic Press. https://doi.org/10.1016/B978-012323841-2/50012-9

Blough, N. V., Zafiriou, O. C., & Bonilla, J. (1993). Optical absorption spectra of waters from the Orinoco River outflow: Terrestrial input of colored organic matter to the Caribbean. *Journal of Geophysical Research*, *98*(C2), 2271–2278. https://doi.org/10.1029/92JC02763

Boss, E., Pegau, W. S., Zaneveld, J. R. V., & Barnard, A. H. (2001). Spatial and temporal variability of absorption by dissolved material at a continental shelf. *Journal of Geophysical Research*, *106*(C5), 9499–9507. https://doi.org/10.1029/2000JC900008

Bricaud, A., Morel, A., & Prieur, L. (1981). Absorption by dissolved organic matter of the sea (yellow substance) in the UV and visible domains1. *Limnology & Oceanography*, *26*(1), 43–53. https://doi.org/10.4319/lo.1981.26.1.0043

Cao, F., Tzortziou, M., Hu, C., Mannino, A., Fichot, C. G., Del Vecchio, R., et al. (2018). Remote sensing retrievals of colored dissolved organic matter and dissolved organic carbon dynamics in North American estuaries and their margins. *Remote Sensing of Environment*, *205*, 151–165. https://doi.org/10.1016/j.rse.2017.11.014

Carlson, C., Hooker, S., Mannino, A., McClain, C., Nelson, N., & Siegel, D. (1999). CLIVAR [Dataset]. *SeaWiFS Bio-optical Archive and Storage System (SeaBASS), NASA*. https://doi.org/10.5067/SeaBASS/CLIVAR/DATA001

Cartisano, C. M., Del Vecchio, R., Bianca, M. R., & Blough, N. V. (2018). Investigating the sources and structure of chromophoric dissolved organic matter (CDOM) in the North Pacific Ocean (NPO) utilizing optical spectroscopy combined with solid phase extraction and borohydride reduction. *Marine Chemistry*, *204*, 20–35. https://doi.org/10.1016/j.marchem.2018.05.005

Catalá, T. S., Reche, I., Álvarez, M., Khatiwala, S., Guallart, E. F., Benítez-Barrios, V. M., et al. (2015). Water mass age and aging driving chromophoric dissolved organic matter in the dark global ocean. *Global Biogeochemical Cycles*, *29*(7), 917–934. https://doi.org/10.1002/2014GB005048

Catalá, T. S., Reche, I., Fuentes-Lema, A., Romera-Castillo, C., Nieto-Cid, M., Ortega-Retuerta, E., et al. (2015). Turnover time of fluorescent dissolved organic matter in the dark global ocean. *Nature Communications*, *6*(1), 5986. https://doi.org/10.1038/ncomms6986

Chen, X., Wei, W., Xiao, X., Wallace, D., Hu, C., Zhang, L., et al. (2022). Heterogeneous viral contribution to dissolved organic matter processing in a long-term macrocosm experiment. *Environment International*, *158*, 106950. https://doi.org/10.1016/j.envint.2021.106950

Clark, J. B., Mannino, A., Tzortziou, M., Spencer, R. G. M., & Hernes, P. (2022). The transformation and export of organic carbon across an Arctic River-Delta-Ocean continuum. *Journal of Geophysical Research: Biogeosciences*, *127*(12), e2022JG007139. https://doi.org/10.1029/2022JG007139

Coble, P. G. (2007). Marine optical biogeochemistry: The chemistry of ocean color. *Chemical Reviews*, *107*(2), 402–418. https://doi.org/10.1021/cr050350+

de Boyer Montégut, C., Madec, G., Fischer, A. S., Lazar, A., & Iudicone, D. (2004). Mixed layer depth over the global ocean: An examination of profile data and a profile-based climatology. *Journal of Geophysical Research*, *109*(C12). C12003. https://doi.org/10.1029/2004JC002378

De La Fuente, P., Marrasé, C., Canepa, A., Antón Álvarez-Salgado, X., Gasser, M., Fajar, N. M., et al. (2014). Does a general relationship exist between fluorescent dissolved organic matter and microbial respiration?–The case of the dark equatorial Atlantic Ocean. *Deep Sea Research Part I: Oceanographic Research Papers*, *89*, 44–55. https://doi.org/10.1016/j.dsr.2014.03.007

Del Castillo, C. E., & Miller, R. L. (2008). On the use of ocean color remote sensing to measure the transport of dissolved organic carbon by the Mississippi River Plume. *Remote Sensing of Environment*, *112*(3), 836–844. https://doi.org/10.1016/j.rse.2007.06.015

Del Vecchio, R., & Blough, N. V. (2004). Spatial and seasonal distribution of chromophoric dissolved organic matter and dissolved organic carbon in the Middle Atlantic Bight. *Marine Chemistry*, *89*(1), 169–187. https://doi.org/10.1016/j.marchem.2004.02.027

Del Vecchio, R., & Subramaniam, A. (2004). Influence of the Amazon River on the surface optical properties of the western tropical North Atlantic Ocean. *Journal of Geophysical Research*, *109*(C11). C11001. https://doi.org/10.1029/2004JC002503

DeVries, T. (2014). The oceanic anthropogenic CO_2 sink: Storage, air-sea fluxes, and transports over the industrial era. *Global Biogeochemical Cycles*, *28*(7), 631–647. https://doi.org/10.1002/2013GB004739

DeVries, T. (2022). Atmospheric CO_2 and sea surface temperature variability cannot explain recent decadal variability of the ocean CO_2 sink. *Geophysical Research Letters*, *49*(7), e2021GL096018. https://doi.org/10.1029/2021GL096018

DeVries, T., & Primeau, F. (2011). Dynamically and observationally constrained estimates of water-mass distributions and ages in the global ocean. *Journal of Physical Oceanography*, *41*(12), 2381–2401. https://doi.org/10.1175/JPO-D-10-05011.1

Dittmar, T., & Kattner, G. (2003). The biogeochemistry of the river and shelf ecosystem of the Arctic Ocean: A review. *Marine Chemistry*, *83*(3), 103–120. https://doi.org/10.1016/S0304-4203(03)00105-1

Dutkiewicz, S., Hickman, A. E., Jahn, O., Henson, S., Beaulieu, C., & Monier, E. (2019). Ocean colour signature of climate change. *Nature Communications*, *10*(1), 578. https://doi.org/10.1038/s41467-019-08457-x

Fichot, C. G., Tzortziou, M., & Mannino, A. (2023). Remote sensing of dissolved organic carbon (DOC) stocks, fluxes and transformations along the land-ocean aquatic continuum: Advances, challenges, and opportunities. *Earth-Science Reviews*, *242*, 104446. https://doi.org/10.1016/j.earscirev.2023.104446

Garver, S. A., & Siegel, D. A. (1997). Inherent optical property inversion of ocean color spectra and its biogeochemical interpretation: 1. Time series from the Sargasso Sea. *Journal of Geophysical Research*, *102*(C8), 18607–18625. https://doi.org/10.1029/96JC03243

Hansell, D. A. (2013). Recalcitrant dissolved organic carbon fractions. *Annual Review of Marine Science*, *5*(1), 421–445. https://doi.org/10.1146/annurev-marine-120710-100757

Holzer, M., DeVries, T., & de Lavergne, C. (2021). Diffusion controls the ventilation of a Pacific Shadow Zone above abyssal overturning. *Nature Communications*, *12*(1), 4348. https://doi.org/10.1038/s41467-021-24648-x

Hu, C., Lee, Z., Muller-Karger, E., Carder, L., & Walsh, J. J. (2006). Ocean color reveals phase shift between marine plants and yellow substance. *IEEE Geoscience and Remote Sensing Letters*, *3*(2), 262–266. https://doi.org/10.1109/LGRS.2005.862527

Huang, J., Chen, J., Wu, M., Gong, L., & Zhang, X. (2022). Estimation of chromophoric dissolved organic matter and its controlling factors in Beaufort Sea using mixture density network and Sentinel-3 data. *The Science of the Total Environment*, *849*, 157677. https://doi.org/10.1016/j.scitotenv.2022.157677

Iuculano, F., Álverez-Salgado, X. A., Otero, J., Catalá, T. S., Sobrino, C., Duarte, C. M., & Agustí, S. (2019). Patterns and drivers of UV absorbing chromophoric dissolved organic matter in the euphotic layer of the open ocean. *Frontiers in Marine Science*, *6*, 320. https://doi.org/10.3389/fmars.2019.00320

Jørgensen, L., Stedmon, C. A., Kragh, T., Markager, S., Middelboe, M., & Søndergaard, M. (2011). Global trends in the fluorescence characteristics and distribution of marine dissolved organic matter. *Marine Chemistry*, *126*(1), 139–148. https://doi.org/10.1016/j.marchem.2011.05.002

Kaiser, K., Benner, R., & Amon, R. M. W. (2017). The fate of terrigenous dissolved organic carbon on the Eurasian shelves and export to the North Atlantic. *Journal of Geophysical Research: Oceans*, *122*(1), 4–22. https://doi.org/10.1002/2016JC012380

Kim, J., & Kim, G. (2015). Importance of colored dissolved organic matter (CDOM) inputs from the deep sea to the euphotic zone: Results from the East (Japan) Sea. *Marine Chemistry*, *169*, 33–40. https://doi.org/10.1016/j.marchem.2014.12.010

Kim, J., & Kim, G. (2016). Significant anaerobic production of fluorescent dissolved organic matter in the deep East Sea (Sea of Japan). *Geophysical Research Letters*, *43*(14), 7609–7616. https://doi.org/10.1002/2016GL069335

Kwon, E. Y., DeVries, T., Galbraith, E. D., Hwang, J., Kim, G., & Timmermann, A. (2021). Stable carbon isotopes suggest large terrestrial carbon inputs to the global ocean. *Global Biogeochemical Cycles*, *35*(4), e2020GB006684. https://doi.org/10.1029/2020GB006684

Li, Y., Song, G., Massicotte, P., Yang, F., Li, R., & Xie, H. (2019). Distribution, seasonality, and fluxes of dissolved organic matter in the Pearl River (Zhujiang) Estuary, China. *Biogeosciences*, *16*(13), 2751–2770. https://doi.org/10.5194/bg-16-2751-2019

Lønborg, C., Álvarez-Salgado, X. A., Davidson, K., Martínez-García, S., & Teira, E. (2010). Assessing the microbial bioavailability and degradation rate constants of dissolved organic matter by fluorescence spectroscopy in the coastal upwelling system of the Ría de Vigo. *Marine Chemistry*, *119*(1), 121–129. https://doi.org/10.1016/j.marchem.2010.02.001

Maie, N., Pisani, O., & JaffÉ, R. (2008). Mangrove tannins in aquatic ecosystems: Their fate and possible influence on dissolved organic carbon and nitrogen cycling. *Limnology & Oceanography*, *53*(1), 160–171. https://doi.org/10.4319/lo.2008.53.1.0160

Mannino, A., Russ, M. E., & Hooker, S. B. (2008). Algorithm development and validation for satellite-derived distributions of DOC and CDOM in the U.S. middle Atlantic bight. *Journal of Geophysical Research*, *113*(C7). C07051. https://doi.org/10.1029/2007JC004493

Margolin, A. R., Gonnelli, M., Hansell, D. A., & Santinelli, C. (2018). Black Sea dissolved organic matter dynamics: Insights from optical analyses. *Limnology & Oceanography*, *63*(3), 1425–1443. https://doi.org/10.1002/lno.10791

Maritorena, S., Siegel, D. A., & Peterson, A. R. (2002). Optimization of a semianalytical ocean color model for global-scale applications. *Applied Optics*, *41*(15), 2705–2714. https://doi.org/10.1364/AO.41.002705

Martin, P., Cherukuru, N., Tan, A. S. Y., Sanwlani, N., Mujahid, A., & Müller, M. (2018). Distribution and cycling of terrigenous dissolved organic carbon in peatland-draining rivers and coastal waters of Sarawak, Borneo. *Biogeosciences*, *15*(22), 6847–6865. https://doi.org/10.5194/bg-15-6847-2018

Matsuoka, A., Babin, M., Doxaran, D., Hooker, S. B., Mitchell, B. G., Bélanger, S., & Bricaud, A. (2014). A synthesis of light absorption properties of the Arctic ocean: Application to semianalytical estimates of dissolved organic carbon concentrations from space. *Biogeosciences*, *11*(12), 3131–3147. https://doi.org/10.5194/bg-11-3131-2014

Meyers-Schulte, K. J., & Hedges, J. I. (1986). Molecular evidence for a terrestrial component of organic matter dissolved in ocean water. *Nature*, *321*(6065), 61–63. https://doi.org/10.1038/321061a0

Mopper, K., Zhou, X., Kieber, R. J., Kieber, D. J., Sikorski, R. J., & Jones, R. D. (1991). Photochemical degradation of dissolved organic carbon and its impact on the oceanic carbon cycle. *Nature*, *353*(6339), 60–62. https://doi.org/10.1038/353060a0

NASA Goddard Space Flight Center, Ocean Ecology Laboratory, Ocean Biology Processing Group. (2022). Sea-Viewing wide field-of-view Sensor (SeaWiFS) ORBVIEW-2 SEAWIFS level-3 mapped garver-siegel-maritorena model data [Dataset]. *NASA OB.DAAC*. https://doi.org/10.5067/ORBVIEW-2/SEAWIFS/L4M/GSM/2022

Nelson, N. B., & Gauglitz, J. M. (2016). Optical signatures of dissolved organic matter transformation in the global ocean. *Frontiers in Marine Science*, *2*, 118. https://doi.org/10.3389/fmars.2015.00118

Nelson, N. B., & Siegel, D. A. (2013). The global distribution and dynamics of chromophoric dissolved organic matter. *Annual Review of Marine Science*, *5*(1), 447–476. https://doi.org/10.1146/annurev-marine-120710-100751

Nelson, N. B., Siegel, D. A., Carlson, C. A., & Swan, C. M. (2010). Tracing global biogeochemical cycles and meridional overturning circulation using chromophoric dissolved organic matter. *Geophysical Research Letters*, *37*(3). L03610. https://doi.org/10.1029/2009GL042325

Nelson, N. B., Siegel, D. A., Carlson, C. A., Swan, C. M., Smethie, W. M., & Khatiwala, S. (2007). Hydrography of chromophoric dissolved organic matter in the North Atlantic. *Deep Sea Research Part I: Oceanographic Research Papers*, *54*(5), 710–731. https://doi.org/10.1016/j.dsr.2007.02.006

Nelson, N. B., Siegel, D. A., & Michaels, A. F. (1998). Seasonal dynamics of colored dissolved material in the Sargasso Sea. *Deep Sea Research Part I: Oceanographic Research Papers*, *45*(6), 931–957. https://doi.org/10.1016/S0967-0637(97)00106-4

Nowicki, M., DeVries, T., & Siegel, D. A. (2022). Quantifying the carbon export and sequestration pathways of the ocean's biological carbon pump. *Global Biogeochemical Cycles*, *36*(3), e2021GB007083. https://doi.org/10.1029/2021GB007083

Opsahl, S., & Benner, R. (1997). Distribution and cycling of terrigenous dissolved organic matter in the ocean. *Nature*, *386*(6624), 480–482. https://doi.org/10.1038/386480a0

Ortega-Retuerta, E., Siegel, D. A., Nelson, N. B., Duarte, C. M., & Reche, I. (2010). Observations of chromophoric dissolved and detrital organic matter distribution using remote sensing in the Southern Ocean: Validation, dynamics and regulation. *Journal of Marine Systems*, *82*(4), 295–303. https://doi.org/10.1016/j.jmarsys.2010.06.004

Romera-Castillo, C., Sarmento, H., Álvarez-Salgado, X. A., Gasol, J. M., & Marrasé, C. (2011). Net production and consumption of fluorescent colored dissolved organic matter by natural bacterial assemblages growing on marine phytoplankton exudates. *Applied and Environmental Microbiology*, *77*(21), 7490–7498. https://doi.org/10.1128/AEM.00200-11

Romera-Castillo, C., Sarmento, H., Álvarez-Salgado, X. A., Gasol, J. M., & Marraséa, C. (2010). Production of chromophoric dissolved organic matter by marine phytoplankton. *Limnology & Oceanography*, *55*(1), 446–454. https://doi.org/10.4319/lo.2010.55.1.0446

Salisbury, J., Vandemark, D., Campbell, J., Hunt, C., Wisser, D., Reul, N., & Chapron, B. (2011). Spatial and temporal coherence between Amazon River discharge, salinity, and light absorption by colored organic carbon in western tropical Atlantic surface waters. *Journal of Geophysical Research*, *116*(C7). C00H02. https://doi.org/10.1029/2011JC006989

Siegel, D. A., Behrenfeld, M. J., Maritorena, S., McClain, C. R., Antoine, D., Bailey, S. W., et al. (2013). Regional to global assessments of phytoplankton dynamics from the SeaWiFS mission. *Remote Sensing of Environment*, *135*, 77–91. https://doi.org/10.1016/j.rse.2013.03.025

Siegel, D. A., Buesseler, K. O., Doney, S. C., Sailley, S. F., Behrenfeld, M. J., & Boyd, P. W. (2014). Global assessment of ocean carbon export by combining satellite observations and food-web models. *Global Biogeochemical Cycles*, *28*(3), 181–196. https://doi.org/10.1002/2013GB004743

Siegel, D. A., Maritorena, S., Nelson, N. B., Hansell, D. A., & Lorenzi-Kayser, M. (2002). Global distribution and dynamics of colored dissolved and detrital organic materials. *Journal of Geophysical Research*, *107*(C12), 3228. https://doi.org/10.1029/2001JC000965

Spencer, R. G. M., Aiken, G. R., Wickland, K. P., Striegl, R. G., & Hernes, P. J. (2008). Seasonal and spatial variability in dissolved organic matter quantity and composition from the Yukon River basin, Alaska. *Global Biogeochemical Cycles*, *22*(4), GB4002. https://doi.org/10.1029/2008GB003231

Stedmon, C. A., & Nelson, N. B. (2015). The optical properties of DOM in the ocean. In *Biogeochemistry of marine dissolved organic matter* (pp. 481–508). Elsevier. https://doi.org/10.1016/B978-0-12-405940-5.00010-8

Stedmon, C. A., Thomas, D. N., Granskog, M., Kaartokallio, H., Papadimitriou, S., & Kuosa, H. (2007). Characteristics of dissolved organic matter in Baltic coastal sea ice: Allochthonous or autochthonous origins? *Environmental Science & Technology*, *41*(21), 7273–7279. https://doi.org/10.1021/es071210f

Steinberg, D. K., Nelson, N. B., Carlson, C. A., & Prusak, A. (2004). Production of chromophoric dissolved organic matter (CDOM) in the open ocean by zooplankton and the colonial cyanobacterium Trichodesmium spp. *Marine Ecology Progress Series*, *267*, 45–56. https://doi.org/10.3354/meps267045

Stubbins, A., & Dittmar, T. (2015). Illuminating the deep: Molecular signatures of photochemical alteration of dissolved organic matter from North Atlantic Deep Water. *Marine Chemistry*, *177*, 318–324. https://doi.org/10.1016/j.marchem.2015.06.020

Swan, C. M., Nelson, N. B., Siegel, D. A., & Fields, E. A. (2013). A model for remote estimation of ultraviolet absorption by chromophoric dissolved organic matter based on the global distribution of spectral slope. *Remote Sensing of Environment*, *136*, 277–285. https://doi.org/10.1016/j.rse.2013.05.009

Swan, C. M., Nelson, N. B., Siegel, D. A., & Kostadinov, T. S. (2012). The effect of surface irradiance on the absorption spectrum of chromophoric dissolved organic matter in the global ocean. *Deep Sea Research Part I: Oceanographic Research Papers*, *63*, 52–64. https://doi.org/10.1016/j.dsr.2012.01.008

Swan, C. M., Siegel, D. A., Nelson, N. B., Carlson, C. A., & Nasir, E. (2009). Biogeochemical and hydrographic controls on chromophoric dissolved organic matter distribution in the Pacific Ocean. *Deep Sea Research Part I: Oceanographic Research Papers*, *56*(12), 2175–2192. https://doi.org/10.1016/j.dsr.2009.09.002

Vodacek, A., Blough, N. V., DeGrandpre, M. D., DeGrandpre, M. D., & Nelson, R. K. (1997). Seasonal variation of CDOM and DOC in the middle Atlantic Bight: Terrestrial inputs and photooxidation. *Limnology & Oceanography*, *42*(4), 674–686. https://doi.org/10.4319/lo.1997.42.4.0674

Werdell, P. J., McKinna, L. I. W., Boss, E., Ackleson, S. G., Craig, S. E., Gregg, W. W., et al. (2018). An overview of approaches and challenges for retrieving marine inherent optical properties from ocean color remote sensing. *Progress in Oceanography*, *160*, 186–212. https://doi.org/10.1016/j.pocean.2018.01.001

Yamashita, Y., Nishioka, J., Obata, H., & Ogawa, H. (2020). Shelf humic substances as carriers for basin-scale iron transport in the North Pacific. *Scientific Reports*, *10*(1), 4505. https://doi.org/10.1038/s41598-020-61375-7

Yamashita, Y., & Tanoue, E. (2003). Chemical characterization of protein-like fluorophores in DOM in relation to aromatic amino acids. *Marine Chemistry*, *82*(3), 255–271. https://doi.org/10.1016/S0304-4203(03)00073-2

Yamashita, Y., & Tanoue, E. (2008). Production of bio-refractory fluorescent dissolved organic matter in the ocean interior. *Nature Geoscience*, *1*(9), 579–582. https://doi.org/10.1038/ngeo279

Yang, L., Choi, J. H., & Hur, J. (2014). Benthic flux of dissolved organic matter from lake sediment at different redox conditions and the possible effects of biogeochemical processes. *Water Research*, *61*, 97–107. https://doi.org/10.1016/j.watres.2014.05.009

Zhao, Z., Gonsior, M., Luek, J., Timko, S., Ianiri, H., Hertkorn, N., et al. (2017). Picocyanobacteria and deep-ocean fluorescent dissolved organic matter share similar optical properties. *Nature Communications*, *8*(1), 15284. https://doi.org/10.1038/ncomms15284

References From the Supporting Information

Astoreca, R., Rousseau, V., & Lancelot, C. (2009). Coloured dissolved organic matter (CDOM) in Southern North Sea waters: Optical characterization and possible origin. *Estuarine, Coastal and Shelf Science*, *85*(4), 633–640. https://doi.org/10.1016/j.ecss.2009.10.010

Battin, T. J. (1998). Dissolved organic matter and its optical properties in a blackwater tributary of the upper Orinoco River, Venezuela. *Organic Geochemistry*, *28*(9), 561–569. https://doi.org/10.1016/S0146-6380(98)00028-X

Bhattacharya, R., & Osburn, C. L. (2021). Chromophoric dissolved organic matter composition and load from a coastal river system under variable flow regimes. *The Science of the Total Environment*, *760*, 143414. https://doi.org/10.1016/j.scitotenv.2020.143414

Cao, F., Medeiros, P. M., & Miller, W. L. (2016). Optical characterization of dissolved organic matter in the Amazon River plume and the Adjacent Ocean: Examining the relative role of mixing, photochemistry, and microbial alterations. *Marine Chemistry*, *186*, 178–188. https://doi.org/10.1016/j.marchem.2016.09.007

Chen, Z., Li, Y., & Pan, J. (2004). Distributions of colored dissolved organic matter and dissolved organic carbon in the Pearl River Estuary, China. *Continental Shelf Research*, *24*(16), 1845–1856. https://doi.org/10.1016/j.csr.2004.06.011

Costa, M. P. F., Novo, E. M. L. M., & Telmer, K. H. (2013). Spatial and temporal variability of light attenuation in large rivers of the Amazon. *Hydrobiologia*, *702*(1), 171–190. https://doi.org/10.1007/s10750-012-1319-2

Fichot, C. G., & Benner, R. (2012). The spectral slope coefficient of chromophoric dissolved organic matter (S275–295) as a tracer of terrigenous dissolved organic carbon in river-influenced ocean margins. *Limnology & Oceanography*, *57*(5), 1453–1466. https://doi.org/10.4319/lo.2012.57.5.1453

Guo, W., Stedmon, C. A., Han, Y., Wu, F., Yu, X., & Hu, M. (2007). The conservative and non-conservative behavior of chromophoric dissolved organic matter in Chinese estuarine waters. *Marine Chemistry*, *107*(3), 357–366. https://doi.org/10.1016/j.marchem.2007.03.006

Guo, W., Yang, L., Zhai, W., Chen, W., Osburn, C. L., Huang, X., & Li, Y. (2014). Runoff-mediated seasonal oscillation in the dynamics of dissolved organic matter in different branches of a large bifurcated estuary—The changjiang estuary. *Journal of Geophysical Research: Biogeosciences*, *119*(5), 776–793. https://doi.org/10.1002/2013JG002540

Hernes, P. J., & Benner, R. (2003). Photochemical and microbial degradation of dissolved lignin phenols: Implications for the fate of terrigenous dissolved organic matter in marine environments. *Journal of Geophysical Research*, *108*(C9), 3291. https://doi.org/10.1029/2002JC001421

Kowalczuk, P., Cooper, W. J., Whitehead, R. F., Durako, M. J., & Sheldon, W. (2003). Characterization of CDOM in an organic-rich river and surrounding coastal ocean in the South Atlantic Bight. *Aquatic Sciences*, *65*(4), 384–401. https://doi.org/10.1007/s00027-003-0678-1

Nieke, B., Reuter, R., Heuermann, R., Wang, H., Babin, M., & Therriault, J. C. (1997). Light absorption and fluorescence properties of chromophoric dissolved organic matter (CDOM), in the St. Lawrence Estuary (Case 2 waters). *Continental Shelf Research*, *17*(3), 235–252. https://doi.org/10.1016/S0278-4343(96)00034-9

Palacios, S. L., Peterson, T. D., & Kudela, R. M. (2009). Development of synthetic salinity from remote sensing for the Columbia River plume. *Journal of Geophysical Research*, *114*(C2), C00B05. https://doi.org/10.1029/2008JC004895

Rochelle-Newall, E. J., & Fisher, T. R. (2002). Chromophoric dissolved organic matter and dissolved organic carbon in Chesapeake Bay. *Marine Chemistry*, *77*(1), 23–41. https://doi.org/10.1016/S0304-4203(01)00073-1

Song, G., Li, Y., Hu, S., Li, G., Zhao, R., Sun, X., & Xie, H. (2017). Photobleaching of chromophoric dissolved organic matter (CDOM) in the yangtze river estuary: Kinetics and effects of temperature, pH, and salinity. *Environmental Sciences: Processes and Impacts*, *19*(6), 861–873. https://doi.org/10.1039/C6EM00682E

Spencer, R. G. M., Stubbins, A., Hernes, P. J., Baker, A., Mopper, K., Aufdenkampe, A. K., et al. (2009). Photochemical degradation of dissolved organic matter and dissolved lignin phenols from the Congo River. *Journal of Geophysical Research*, *114*(G3). https://doi.org/10.1029/2009JG000968

Spencer, R. G. M., Aiken, G. R., Dornblaser, M. M., Butler, K. D., Holmes, R. M., Fiske, G., et al. (2013). Chromophoric dissolved organic matter export from U.S. rivers. *Geophysical Research Letters*, *40*(8), 1575–1579. https://doi.org/10.1002/grl.50357

Sun, Q., Wang, C., Wang, P., Hou, J., & Ao, Y. (2014). Absorption and fluorescence characteristics of chromophoric dissolved organic matter in the Yangtze Estuary. *Environmental Science and Pollution Research*, *21*(5), 3460–3473. https://doi.org/10.1007/s11356-013-2287-4

de Matos Valerio, A., Kampel, M., Vantrepotte, V., Ward, N. D., Sawakuchi, H. O., Less, D. F. D. S., et al. (2018). Using CDOM optical properties for estimating DOC concentrations and pCO_2 in the Lower Amazon River. *Optics Express*, *26*(14), A657–A677. https://doi.org/10.1364/OE.26.00A657

Xie, H., Aubry, C., Bélanger, S., & Song, G. (2012). The dynamics of absorption coefficients of CDOM and particles in the St. Lawrence estuarine system: Biogeochemical and physical implications. *Marine Chemistry*, *128–129*, 44–56. https://doi.org/10.1016/j.marchem.2011.10.001

Yu, X., Shen, F., & Liu, Y. (2016). Light absorption properties of CDOM in the Changjiang (Yangtze) estuarine and coastal waters: An alternative approach for DOC estimation. *Estuarine, Coastal and Shelf Science*, *181*, 302–311. https://doi.org/10.1016/j.ecss.2016.09.004

Zhu, W.-Z., Zhang, J., & Yang, G.-P. (2018). Mixing behavior and photobleaching of chromophoric dissolved organic matter in the Changjiang River estuary and the adjacent East China Sea. *Estuarine, Coastal and Shelf Science*, *207*, 422–434. https://doi.org/10.1016/j.ecss.2017.07.019